An experimentally-determined general formalism for evaporation and isotope fractionation of Cu and Zn from silicate melts between 1300 and 1500 °C and 1 bar

Paolo Sossi, Frederic Moynier, Robin Treilles, Marwane Mokhtari, Xiang Wang, Julien Siebert

An experimentally-determined general formalism for evaporation and isotope fractionation of Cu and Zn from silicate melts between 1300 - 1500 °C and 1 bar

Paolo A. Sossi[1, 2*], Frédéric Moynier[1], Robin Treilles[1], Marwane Mokhtari[1], Xiang Wang[1], Julien Siebert[1]

[1] Institut de Physique du Globe de Paris, 1 rue Jussieu, F-75005, Paris, France

[2] Institute of Geochemistry and Petrology, ETH Zürich, Sonneggstrasse 5, CH-8092, Zürich, Switzerland

* corresponding author. E-mail: paolo.sossi@erdw.ethz.ch

Abstract

Vaporisation fractionates elements and their isotopes between condensed phase(s) and the gas phase according to two end-member regimes; kinetic (Langmuir) or equilibrium (Knudsen). The fractionation factor of isotopes *i* and *j* of element E between gas and liquid, $^{i/j}\mathrm{E}(\alpha_{vap\text{-}liq})$, in the former case depends only on the molar masses of the evaporating species, $(M_j/M_i)^{0.5}$, whereas, at equilibrium, fractionation is ~1 at high temperatures. The prevailing regime depends on the production rate of vapour species relative to their rate of transport away from the evaporating surface, for which an accurate theory is lacking. Here, we present results of Cu and Zn isotope fractionation during evaporation of ferrobasaltic melts in the $\mathrm{FeO^{(T)}}$-CaO-MgO-$\mathrm{Al_2O_3}$-$\mathrm{SiO_2}$ (FCMAS) system in a 1 atm gas-mixing furnace at oxygen fugacities ($f\mathrm{O_2}$) from 10^{-8} bar to $10^{-0.68}$ bar (air) at temperatures between 1300 and 1500 °C. In air, the fractionation factors are $^{65/63}\mathrm{Cu}(\alpha_{vap\text{-}liq}) = 0.9972 \pm 0.0001$ and $^{66/64}\mathrm{Zn}(\alpha_{vap\text{-}liq}) = 0.9959 \pm 0.0002$, but increase under reducing conditions, at $\log f\mathrm{O_2} = -8$ for $^{65/63}\mathrm{Cu}(\alpha_{vap\text{-}liq})$ (0.9979) and at -3, -5.5 and -8 for Zn, at which $^{66/64}\mathrm{Zn}(\alpha_{vap\text{-}liq}) = 0.9967$, 0.9974 and 0.9978, respectively. This behaviour is caused by slow elemental diffusion through the silicate melt relative to the rate of evaporative loss, thereby depressing $^{i/j}\mathrm{E}(\alpha_{vap\text{-}liq})$. When evaporation rates far exceed those for diffusion in the melt, no isotopic fractionation develops in the condensed phase. To account for the $^{65/63}\mathrm{Cu}(\alpha_{vap\text{-}liq})$ and $^{66/64}\mathrm{Zn}(\alpha_{vap\text{-}liq})$ values observed in air, we develop a formalism for mass transfer applicable to any evaporating species over a range of pressures, gas compositions and flow regimes. For natural convection at 1 bar, diffusive transport through the gas is the rate-limiting step, where $D_{(i,j)k}$ is the diffusion of isotope *i* or *j* through a gas with mean molar mass M_k. Under these conditions $^{i/j}\mathrm{E}(\alpha_{vap\text{-}liq})$ is proportional to $(D_{ik}/D_{jk})^{2/3}$, and not (D_{ik}/D_{jk}) as previously suggested. Our model predicts $^{i/j}\mathrm{E}(\alpha_{vap\text{-}liq})$ in other experiments, and in nature, to a precision of ± 0.0005 assuming ideality. The fractionation factors inferred for moderately volatile elements in lunar mare basalts (>0.9994) are inconsistent with a mass transport process, and instead reflect near-equilibrium conditions of vapour loss from the Moon.

Key words: Evaporation, Vapour, Cu, Zn, Silicate melt

Word count: 11441 (not including references, tables, figure captions, appendices).

Figures: 11

Tables: 4

1.0. Introduction

The phase transition from liquid- to gas, termed evaporation, is commonplace in geological processes. Because the gas phase, as quantified by the ideal gas law, is less dense than condensed phases, mass transport occurs more rapidly such that it readily escapes the system, leaving the residue depleted in volatile components.

Two end-members styles of evaporation are classified according to the ease with which the gas phase escapes (Fuchs, 1959; Chapman and Cowling, 1970). In natural processes, evaporation may fall anywhere between the Langmuir (kinetic) and Knudsen (equilibrium) regimes. The former occurs when each parcel of evaporating gas is perfectly and instantaneously removed from the evaporating surface, and evaporation rate is therefore at a maximum (Langmuir, 1916). Knudsen evaporation, by contrast, takes place when the vapour pressure of the evaporating species at the surface is equal to the equilibrium partial pressure, such that the system has reached an equilibrium state (Knudsen, 1909). Physically, these two regimes predominate for evaporation into a vacuum where gas escapes readily (Langmuir) or in a closed system where the gas phase remains in contact with the condensed phase(s) (Knudsen). The geological importance lies in the potential for the evaporative regime to give rise to different chemical and isotopic signatures in the condensed phase (*e.g.,* Davis et al., 1990; Hashimoto, 1990; Humayun and Cassen, 2000; Day and Moynier, 2014).

At high temperatures, the isotopic fractionation of volatile elements in geological materials is an ideal record of evaporative style. This is because, for pure Langmuir evaporation, fractionation in the abundances, X, of two isotopes, i and j of element E, between liquid (*liq*) and vapour (*vap*), defined as:

$$^{i/j}E(\alpha_{vap-liq}) = \frac{(\,^{i}X_E/\,^{j}X_E)_{vap}}{(\,^{i}X_E/\,^{j}X_E)_{liq}}, \quad (1)$$

is predictable as the inverse square root of the molar masses (M) of the evaporating species; $(M_j/M_i)^{0.5}$. For the naturally-occurring isotopes, this quantity lies between 0.707 (H/D) and 0.998 ($^{207}Pb/^{208}Pb$). Conversely, the isotopic fractionation at equilibrium is controlled only by the ratio of the equilibrium partial pressures of the two isotopes; $p_{i,eq}/p_{j,eq}$, which, at high temperatures, is very near unity. Therefore, isotopic fractionation caused by Langmuir evaporation is considerably larger than for Knudsen evaporation.

In a geo- and cosmochemical context, semi-volatile metals, such as Cu, Zn and K (Palme et al., 1988; Sossi and Fegley, 2018) provide useful insight into such processes, because of their balanced partitioning between vapour and condensed phases. That the isotopic fractionation of potassium observed in meteorites by Humayun and Clayton (1995) was negligible within the analytical uncertainty (± 0.5 ‰) was used to argue against Langmuir vaporisation as the predominant regime of vapour loss in the solar nebula. This result was surprising, considering that the total pressures at the solar nebular mid-plane were sufficiently low (~10^{-4} bar; Boss, 1998) so as to have facilitated near-pure Langmuir evaporation.

Although subsequent studies with improved mass spectrometric methods were able to identify isotopic fractionation in semi-volatile elements among a variety of terrestrial- and extraterrestrial materials (Poitrasson et al., 2004; Luck et al., 2005; Moynier et al., 2006; Wombacher et al., 2008; Moynier et al., 2009; Wang and Jacobsen 2016; Pringle and Moynier 2017), the fractionation factors inferred for these processes were still much smaller than anticipated for evaporation into a vacuum. These results precipitated renewed interest in the experimental characterisation of isotopic fractionation of semi-volatile elements, particularly K, Mg and Si, in silicate melts of planetary materials under vacuum conditions (Richter et al., 2002; Yu et al., 2003; Richter et al., 2007; Knight et al., 2009; Mendybaev et al., 2017). Through experiment, isotopic fractionation factors in multicomponent silicate systems never reached that expected for the ideal Langmuir case, $(M_j/M_i)^{0.5}$ (although see Dauphas et al. 2004 for

simple systems), and instead were observed to be closer to unity due to modification by *i)* the kinetics of vaporisation, related to the energy barrier associated with evaporation at the surface (Hashimoto, 1990; Richter et al. 2002) and *ii)* the total pressure and mean molar mass of the gas medium into which evaporation occurred (Richter et al. 2011).

The smaller isotopic fractionation factors relative to the Langmuir case inferred for semi-volatile elements in lunar mare basalts (Paniello et al., 2012; Wang and Jacobsen, 2016; Boyce et al., 2018) led to the realisation that isotopic signatures recorded in natural rocks are sensitive to the conditions at which evaporation occurred. Wang and Jacobsen (2016) concluded that K loss during the Moon-forming giant impact must have taken place at high total pressures in order to dampen the isotopic fractionation factor from the Langmuir value $(M_{39}/M_{41})^{0.5} = 0.9753$ expected in a vacuum, to the ~0.9998 observed. A similar fractionation factor is also observed in Zn- (Paniello et al., 2012; Kato et al., 2015) and Cu isotopes (Day et al., 2019) of mare basalts, suggesting that this is a general feature of evaporation during high temperature processes.

Indeed, diminished isotope fractionation factors between vapour and liquid are also recorded in recent impact melt glasses on Earth, formed *via* both asteroidal impacts (tektites, Moynier et al., 2009; Rodovska et al., 2017; Creech et al., 2019, melt sheets, Kamber and Schoenberg, 2020) and nuclear detonation (trinitites, Day et al., 2017) in which ${}^{i/j}E(\alpha_{vap\text{-}liq}) \geq 0.998$. To place these results into context, Wimpenny et al. (2019), subjected silica-rich compositions, taken to approximate the upper continental-crustal source rocks of terrestrial impact melts, to temperatures between 1600 and 2200 °C in an Ar atmosphere. Although the experimentally-measured fractionation factors, $0.9988 < {}^{66/64}Zn(\alpha_{vap\text{-}liq}) < 0.9998$, span those observed in impact melt glasses, the influence of thermodynamic- (oxygen fugacity, temperature) relative to kinetic variables (mass transport in the gas phase, diffusion in the liquid) on the fractionation factor is yet to be quantitatively addressed.

In order to characterise the effects of the evaporative regime on isotopic fractionation of semi-volatile metals from silicate melts, we present results of Cu and Zn vaporisation experiments under controlled thermodynamic conditions in a vertical tube furnace at a total pressure of 1 bar and known gas composition, which is independently varied to explore the effect of oxygen fugacity. We build on the combined thermodynamic-theoretical framework established in Sossi et al., (2019) to develop a formalism for the effect of mass transport of the gas phase on the vaporisation rate, in order to model the chemical and isotopic effects of evaporation in natural processes in a predictive manner. We apply our models to assess the likely regimes of evaporative loss that were extant during tektite formation and on the Moon.

2.0. Methods

2.1. Experimental

Starting materials were made from a combination of high purity (>99.9 %) oxide powders of SiO_2, Al_2O_3, MgO, $CaCO_3$, and Fe_2O_3 in proportions of the anorthite-diopside eutectic ($An_{42}Di_{58}$) with ~15 *wt. %* forsterite and ~15 *wt. %* Fe_2O_3 to resemble a primitive natural basalt with a liquidus temperature ~ 1300 °C (O'Neill and Eggins, 2002; Sossi et al., 2019). The powders were mixed together three times in an agate mortar under acetone, and the ensemble was then fired overnight in a 1 atm box furnace at 1000 °C in air to decarbonate the mixture. The oxides of Cu and Zn were then added as oxides in order to achieve ~20,000 ppm in the final mixture (Cu-Zn mix) or ~1000 ppm (Metalloids mix). The powders were mixed into a slurry using 100,000 molecular weight polyethylene oxide and water, and ~25 mg was smeared onto noble metal wire loops (Pt, except for experiments at or below $\log fO_2$ -5.5, for which Re was used).

Experiments were performed in a 1 atm GERO vertical furnace with a 4.2 cm-diameter alumina tube, heated by $MoSi_2$ elements housed at the Institut de Physique du Globe de Paris (Sossi et al., 2019). The

wire loops were inserted directly into the ~3 cm-long furnace hotspot at the set temperature and desired fO_2. Temperature was digitally monitored and adjusted as necessary with a Tektronix 2110 5½ Digit Multimeter connected to a Type B ($Pt_{70}Rh_{30}$-$Pt_{94}Rh_6$) thermocouple bead placed <5 mm above the sample, with temperature externally set by a Eurotherm ® controller found to be stable to better than ± 0.5 °C. Oxygen fugacity was allowed to equilibrate for ~10 minutes prior to sample introduction and was controlled by CO-CO_2 gas mixing, metered by four MKS G-series mass flow controllers (2 with 500 sccm full scale for CO and CO_2, 1 at 50 sccm full scale for CO, and 1 at 10 sccm full scale for CO_2). The mass flow controllers were calibrated using an $SIRO_2$ oxygen sensor at 1000 °C, giving an uncertainty of ± 0.05 log units at the mixing ratios used in the experiments. Experiments in air were performed under no gas flow. Run time was recorded once the temperature reading at the thermocouple reached ~99% of the set-temperature (~5 minutes) to allow the thermal mass of the sample to equilibrate with the furnace atmosphere. Samples were rapidly quenched by having them drop into a bath of de-ionised water.

2.2. Electron Probe MicroAnalysis

Quenched glass spheres were mounted, together with their wires, in epoxy and sanded down so as to expose the surface of the sphere along its central axis. Electron Probe MicroAnalysis (EPMA) was performed on a Cameca SX-Five Electron Microprobe, housed at CAMPARIS, Université Pierre et Marie Curie, Paris, France. Analyses were carried out with a defocused electron beam of 20 µm accelerated at 15 kV and with a current of 20 nA. X-ray emission was counted by five Wavelength-Dispersive Spectrometers (WDS). The standards used for calibration were: anorthite (Si), albite (Na, Al), periclase (Mg), haematite (Fe), diopside (Ca) and sanidine (K). Phengite was run as an internal standard throughout the sequence to verify the accuracy of the ZAF correction and monitor instrumental drift. Approximately 20 - 40 points per sample were made, including profiles across the sphere in order to detect any zoning in major element composition.

2.3. Laser-Ablation Inductively-Coupled Plasma Mass Spectrometry

The concentrations of Cu and Zn in a subset of the experimental glasses were determined by Laser-Ablation Inductively-Coupled Plasma Mass Spectrometry (LA-ICP-MS) at the Institute of Geochemistry and Petrology, ETH Zürich, Switzerland (Guillong et al., 2014). The polished, epoxy-mounted glasses were placed in a dual-volume Laurin Technics 155 cell filled with a 0.7 L/min He carrier gas. A Resonetics Resolution 193 nm ArF excimer laser with a repetition rate of 4 Hz and a total fluence of 3.5 J/cm^2 was used to ablate spots of 29 µm diameter. The ablation sequence consisted of 20 s background and 40 s of counting time, in which the ablated material was carried to the Thermo Element XR magnetic sector mass spectrometer running in low resolution mode. Each mass peak is measured three times (100 samples per peak with a mass window of 4%) for a total of 0.011 s each. The isotopic masses measured were: ^{7}Li, ^{23}Na, ^{29}Si, ^{39}K, ^{43}Ca, ^{49}Ti, ^{57}Fe, ^{63}Cu, ^{64}Zn, ^{65}Cu, ^{66}Zn, resulting in one sweep every 0.465 s. The ^{232}Th^{16}O/^{232}Th ratio measured during tuning indicates that oxide production was ~ 0.1 %.

Laser spot traverses of ~ 1,200 µm in length consisting of 10 – 12 spots each were performed from the centre of the glass sphere to its edge for three glass beads, 26/12/18a, b, and c. Sample ablation was bracketed by standards every ~20 points, which comprised a sequence of one NIST-610 synthetic glass and two silicate glass standards (BCR-2G and GSD-1G). Standardisation was accomplished by normalisation of the counts per second of a given isotope in the sample glass relative to those in NIST-610 in which Cu and Zn occur at 444 ± 4 ppm and 433 ± 7 ppm, respectively (Eggins and Shelley, 2002). Then, the counts of ^{29}Si were normalised against those obtained by EPMA (41.7 *wt.* % SiO_2 in samples) to correct for different ablation yields of different matrices between ferrobasaltic glasses and NIST-610. Relative standard deviation (RSD) was 1.3% for Cu and 2.0 % for Zn.

2.4. Isotope Ratio Measurement

The glass spheres were broken up and separated from the noble metal wire, before being crushed into a fine powder using an agate mortar. Roughly 5 – 25 mg of powder was dissolved in a mixture of concentrated HNO_3-HCl-HF acids in Teflon beakers for 24 – 48 h at ~130 °C. The chromatographic and mass spectrometric methods follow those outlined in Sossi et al. (2015). Following complete dissolution, the samples were evaporated and re-dissolved in 6M HCl and loaded onto 1 mL of AG1-X8, Cl-form, 200-400 mesh anion exchange resin in high aspect ratio (0.4 cm radius × 7 cm length) Teflon columns. Matrix elements (Mg, Ca, Ti, and most others) are eluted by passage of 5 mL of 6 M HCl, whereas Cu is collected by another 9 mL 6 M HCl. The iron fraction was eluted by 3.5 mL of 0.5 M HCl, while Zn is finally eluted with 4 mL 3 M HNO_3. Total analytical blank quantities of Cu and Zn are 1 ng, and 2 ng, respectively, negligible with respect to typical sample amounts (Cu, Zn ≈ 250 to 400,000 ng).

The isotope composition of Cu and Zn was determined on a Thermo Neptune Plus MC-ICP-MS, housed at the Institut de Physique du Globe de Paris, with nine Faraday cups on 10^{11} Ω resistors. Individual eluates are dissolved in 2% (0.32 M) HNO_3 and introduced into the MC-ICP-MS by means of a 50 µl/min micro-flow glass nebuliser, creating an aqueous aerosol that enters a quartz-glass Scott double-pass cyclonic spray chamber before being ionised by an Ar plasma. Copper and Zn solutions are diluted to 300 ppb. In order to correct for instrumental mass bias, each sample is bracketed by an international reference material (SRM 976 for Cu and JMC-Lyon for Zn), and both samples and standards were doped with an external spike element (Ni for Cu analyses, and Cu for Zn analyses) at the same concentration as the analyte element. Copper and Zn isotope compositions are analysed in low resolution mode on flat-topped peaks. Each analysis consists of 40 integrations of 4.194 s each. Isotope ratios of Cu and Zn are expressed in delta notation, where:

$$\delta^i E = \left(\frac{(\,{}^{i}X_E/\,{}^{j}X_E)_{sample}}{(\,{}^{i}X_E/\,{}^{j}X_E)_{standard}} - 1 \right) \times 1000 \quad (2)$$

The value of i = 66 or 68 for Zn and 65 for Cu, whilst the value of j = 64 for Zn and 63 for Cu. Solutions were run 2 – 3 times each and compared to international reference materials analysed for quality control along with the samples yielding, for BHVO-2, δ^{65}Cu = 0.06 ± 0.03 ‰, δ^{66}Zn = 0.26 ± 0.05 and for BCR-2, δ^{65}Cu = 0.10 ± 0.04 ‰, δ^{66}Zn = 0.29 ± 0.01 ‰, resulting in total analytical uncertainties of ± 0.04 ‰ for δ^{65}Cu and ± 0.06 ‰ for δ^{66}Zn (both 2SD).

207

Table 1. Sample run conditions, their Cu and Zn abundances and isotope compositions relative to the starting material (SM), and modelled log$K$* values.

Sample name	Temperature (°C)	CO (sccm)	CO_2 (sccm)	log fO_2	ΔFMQ	Time (mins)	Loop	Starting mix	Cu (ppm)	ln$f$(Cu)	log$K$*	$\delta^{65}Cu_{SM}$	2SD	N	Zn (ppm)	ln$f$(Zn)	log$K$*	$\delta^{66}Zn_{SM}$	2SD	$\delta^{68}Zn_{SM}$	2SD	N
P 5/04/17b	1500	-	-	-0.68	4.72	60	Pt	Cu-Zn	6580	-0.90	-2.72	2.15	0.02	2	4983	-1.39	-2.7	5.54	0.07	10.79	0.05	2
P 10/04/17a	1500	-	-	-0.68	4.72	15	Pt	Cu-Zn	11113	-0.38	-2.50	1.03	0.02	2	9137	-0.77	-2.36	2.18	0.01	4.24	0.05	2
P10/04/17a-r	1500	-	-	-0.68	4.72	15	Pt	Cu-Zn	11113	-0.38	-2.50	0.92	0.08	2	9137	-0.77	-2.36	2.17	0.06	4.29	0.14	2
P 6/04/17c	1500	-	-	-0.68	4.72	120	Pt	Cu-Zn	3219	-1.61	-2.77	4.39	0.08	2	835	-3.16	-2.65	12.83	0.01	25.23	0.05	2
P 5/04/17a	1400	-	-	-0.68	5.62	60	Pt	Cu-Zn	9694	-0.51	-2.98	1.15	0.06	2	12403	-0.48	-3.18	1.79	0.01	3.58	0.08	2
P 7/04/17b	1400	-	-	-0.68	5.62	15	Pt	Cu-Zn				0.79	0.02	2				0.87	0.02	1.72	0.02	2
P 6/04/17b	1400	-	-	-0.68	5.62	120	Pt	Cu-Zn	6939	-0.85	-3.06	2.03	0.06	2	6884	-1.05	-3.14					
P 4/04/17c	1300	-	-	-0.68	6.62	60	Pt	Cu-Zn	13978	-0.15	-3.54	0.36	0.09	2	16860	-0.16	-3.67	0.67	0.02	1.31	0.05	2
P 6/04/17a	1300	-	-	-0.68	6.62	120	Pt	Cu-Zn	11935	-0.30	-3.52	0.57	0.10	2	13962	-0.35	-3.63	0.94	0.01	1.86	0.09	2
P 7/04/17a	1300	-	-	-0.68	6.62	15	Pt	Cu-Zn	15586	-0.04	-3.51	0.11	0.05	2	18881	-0.04	-3.62	0.30	0.04	0.60	0.04	2
P 31/07/18a	1502	-	200	-2.74	2.64	15	Pt	Cu-Zn	8888	-0.60	-2.72	1.78	0.07	3	6360	-1.13	-2.82	4.17	0.01	8.18	0.09	3
P 31/07/18b	1502	-	20	-2.74	2.64	13	Pt	Cu-Zn	10140	-0.47	-2.77	1.01	0.05	3	6892	-1.05	-2.67	3.25	0.03	6.35	0.04	3
P 21/06/18a	1500	-	200	-2.74	2.66	60	Pt	Metalloids	201	-1.60	-2.99				6	-5.07	-3.17					
P 01/08/18a	1397	-	200	-3.07	3.26	30	Pt	Cu-Zn	8533	-0.64	-3.15	1.60	0.05	3	4697	-1.44	-3.44	4.47	0.04	8.78	0.04	3
P 01/08/18b	1396.6	-	20	-3.07	3.27	29	Pt	Cu-Zn	6628	-0.89	-3.06	2.51	0.04	3	2886	-1.92	-3.29	6.04	0.06	11.78	0.14	3
P 19/06/18d	1400	-	200	-3.07	3.23	60	Pt	Metalloids	545	-0.61	-3.50				100	-2.30	-3.69	7.14	0.01	13.94	0.06	3
P 02/08/18a	1345.5	-	200	-3.26	3.57	55	Pt	Cu-Zn	7427	-0.78	-3.34	1.66	0.06	3	4434	-1.49	-3.85	4.62	0.03	9.09	0.07	3
P 19/06/18a	1299	-	200	-3.44	3.87	67	Pt	Metalloids	682	-0.38	-3.86				533	-0.63	-4.51	1.86	0.09	4.06	0.08	3
P 21/06/18b	1500	16	184	-5.50	-0.10	28	Pt	Metalloids	47	-3.06	-3.06				0.6	-7.42						
P 20/06/18a	1400	5.5	194.5	-5.51	0.79	30	Pt	Metalloids	244	-1.41	-3.45				3	-5.91						
P 22/06/18d	1400	5.5	194.5	-5.51	0.79	10	Pt	Metalloids							12	-4.30	-3.86	9.81*	0.01	19.35*	0.01	3
P 19/06/18b	1299.5	1.6	200	-5.53	1.78	29	Pt	Metalloids	468	-0.76	-3.72				215	-1.40	-4.63	3.40	0.05	6.76	0.02	3
P 01/08/18c	1396.6	6	194	-5.62	0.71	30	Re	Cu-Zn				2.88	0.08	3	5	-8.39		1.39*	0.02	2.69*	0.04	2
P 31/07/18c	1501.7	20	180	-5.70	-0.31	8	Re	Cu-Zn	4279	-1.33	-2.79	3.44	0.02	3	8	-7.83		1.75*	0.01	3.62*	0.15	2
P 3/08/18a	1347	4	196	-5.80	1.02	15	Re	Cu-Zn	7940	-0.71	-3.36	1.68	0.04	3	696	-3.35	-3.85	8.60	0.05	17.01	0.02	3
P 25/07/18a	1398	9.5	190.5	-6.02	0.30	30	Re	Cu-Zn	2277	-1.96	-3.30	5.53	0.03	3	12	-7.38		0.60*	0.07	1.32*	0.03	2
P 03/08/18b	1346.5	40.5	159.5	-7.99	-1.17	30	Re	Cu-Zn	6179	-0.96	-4.11	2.18	0.02	3	122	-5.09	-5.35	11.10	0.03	21.86	0.05	3
P 31/07/18d	1500.5	121.5	78.5	-8.00	-2.60	12	Re	Cu-Zn	303	-3.98	-3.15	8.81	0.07	3	7	-7.98		1.91*	0.11	4.00*	0.18	2
P 19/06/18c	1299	24	176	-8.00	-0.69	17	Re	Metalloids	325	-1.12	-3.93				26	-3.51	-5.11	7.44	0.06	14.54	0.08	2
P 21/06/18c	1500	121.5	78.5	-8.00	-2.60	14	Re	Metalloids	12	-4.42	-3.23				0.5	-7.60						
P 22/06/18b	1500	121.5	78.5	-8.00	-2.60	7	Re	Metalloids							7	-4.81		8.70*	0.08	16.53*	0.10	2
P 20/06/18b	1398	67	133	-8.03	-1.71	13	Re	Metalloids	91	-2.39	-3.48				0.4	-7.82						
P 01/08/18d	1396.6	66.5	133.5	-8.04	-1.70	30	Re	Cu-Zn	62	-5.56	-3.50	11.96	0.09	3	11	-7.45		1.11*	0.01	2.15*	0.04	2
Stand-alone experiments																						
P 26/12/18a	1300	2.7	197.3	-5.99	1.31	10	Re	Cu-Zn	9137	-0.57					9421	-0.54						
P 26/12/18b	1300	2.7	197.3	-5.99	1.31	20	Re	Cu-Zn	4786	-1.22					2860	-1.73						
P 26/12/18c	1300	24	176	-8.00	-0.69	5	Re	Cu-Zn	5321	-1.11					2256	-1.97						

*denotes samples affected by contamination; N = number of replicates; ΔFMQ = log unit deviation in fO_2 from the Fayalite-Magnetite-Quartz buffer; sccm = standard cubic centimetres per minute

208

3.0. Results

3.1. Experimental Glasses

A subset of glasses run at 1300, 1400 and 1500 °C, each at three logfO_2 (-3, -5.5 and -8), totalling nine samples, were analysed for their major element composition by EPMA. Samples at 1400 °C and 1500 °C quenched to glass spheres of ≈ 1000 μm radius; whereas those performed at 1300 °C contained ~5 *wt. %* of olivine ± spinel crystals, as calculated by mass balance. The major element compositions of the wholly glassy experiments (T > 1300 °C) are homogeneous, with an average (expressed as *wt. %* oxide) of 41.70 ± 0.30 SiO_2, 10.60 ± 0.07 Al_2O_3, 15.54 ± 0.11 MgO, 14.58 ± 0.30 FeO^T, and 17.59 ± 0.41 CaO. The composition of each glass is reported in *Supplementary Table S1*.

No zoning in major elements as a function of sphere radius is observed due to their being non-volatile at the experimental conditions. Three standalone experiments were run at 1300 °C for 10 and 20 minutes at logfO_2 = -6, and for 5 minutes at logfO_2 -8, in order to assess the degree of zoning of Cu and Zn at low temperatures and low fO_2, where zoning should be most prevalent because the diffusion rate of the volatile species through the melt decreases with temperature, while evaporation rate increases at more reducing conditions (Sossi et al., 2019). Copper contents vary by <10% between the edge and the centre of experiments run at logfO_2 -6 (Fig. 1a, b), whereas at logfO_2 -8 the outer 300 μm display a decrease in concentration by up to 40 % relative to the interior (Fig. 1c). Zinc concentrations are zoned in all three experiments; with Zn_{rim}/Zn_{core} of 0.8 to 0.7 at logfO_2 -6 (Fig. 1a, b), and more markedly at logfO_2 -8, where they are six times lower in the rim than in the core (Fig. 1c). Data for each zoning profile is presented in *Supplementary Table S2*.

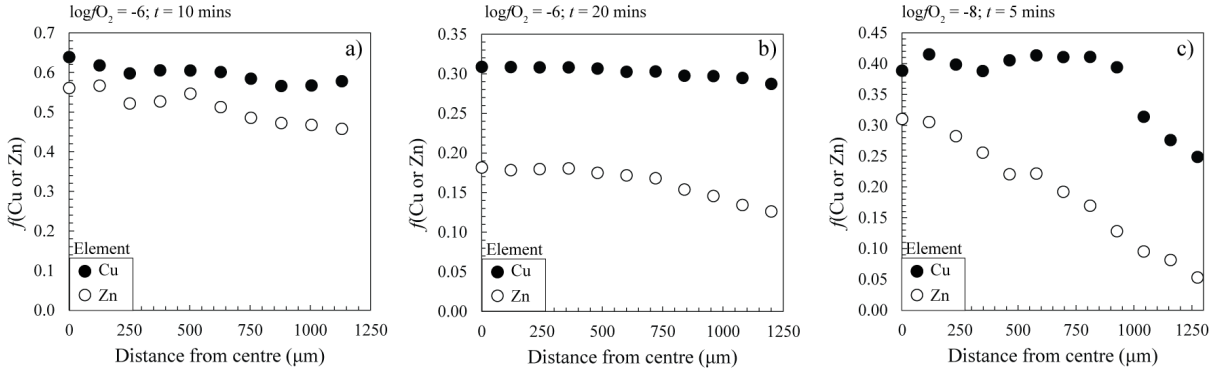

Figure 1. The fraction of Cu or Zn remaining in the glass as a function of distance from the centre of the sphere (in μm) after evaporation at 1300 °C at **a)** logfO_2 = -6, t = 10 minutes, **b)** logfO_2 = -6, t = 20 minutes, and **c)** logfO_2 = -8, t = 5 minutes. Cu = black circles, Zn = white circles.

3.2. Copper and Zinc concentrations

In the two starting mixtures, labelled 'Metalloids' and 'Cu-Zn', Cu is present at 944 ± 12 ppm and 16177 ± 188 ppm, respectively, whereas Zn concentrations are 974 ± 21 ppm and 19747 ± 178 ppm. Bulk copper contents in the experimental glasses of the 'Metalloids' mix are between 682 ppm (run P19/06/18a) and 12 ppm (run P21/06/18c), while those for the 'Cu-Zn mix' fall within the range of 15586 ppm (run P07/04/17a) to 62.3 ppm in run P01/08/18d. Bulk zinc contents of the experimental glasses range from 533 ppm (run P19/06/18a) to 0.5 ppm (run P21/06/18c) in the 'Metalloids' mix and from 18881 ppm (run P07/04/17a) to 4.5 ppm in run P01/08/18c for the 'Cu-Zn' mix (Table 1).

Element depletions in the glasses are expressed as f(E) (E = Cu or Zn), where:

$$f(E) = \frac{X_E^t}{X_E^0} \quad (3)$$

Where X_E refers to the concentration of the element E in the glass at time t and at time 0, respectively.

Calculated values of ln*f*Cu and ln*f*Zn positively co-vary and form discrete linear trends at logfO_2 -0.68 and -3 with intercepts within uncertainty of 0 (Fig. 2). For experiments in air, the relative depletion of Zn relative to Cu (ln*f*Zn/ln*f*Cu) is approximately unity, meaning that both Zn and Cu vaporise to similar extents. The average value is 1.12 ± 0.12 (N = 5) for experiments in air at 1300 °C and 1400 °C, while relatively more Zn depletion is observed for the series at 1500 °C (1.85 ± 0.27, N = 3). This behaviour is predicted thermodynamically for the evaporation of Cu and Zn from basaltic melts, for which the vapour pressure of Zn increases more rapidly with temperature than does that of Cu (Sossi et al., 2019).

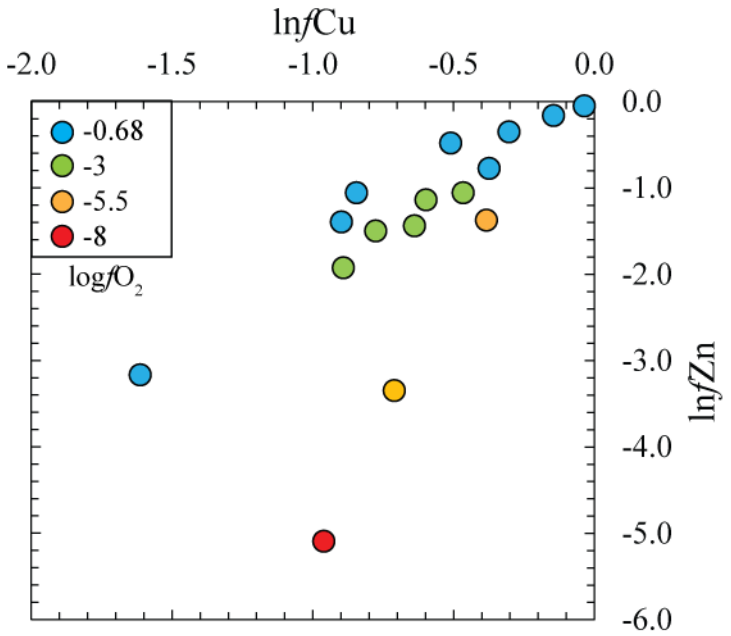

Figure 2. A plot of the natural logarithm of the fraction of Cu remaining in the melt (ln*f*Cu) compared with that of Zn (ln*f*Zn) in a given experiment for the Cu-Zn mix. The points form roughly linear arrays in log-log space for a given fO_2, colour-coded by blue = air, green = pure CO_2 (logfO_2 ~ -3), yellow = logfO_2 -5.5, red = logfO_2 -8. The points qualitatively show that Zn becomes relatively more volatile with respect to Cu at lower fO_2s, as expected according to their reaction stoichiometries. The effect of temperature is to favour Zn loss relative to Cu, though this is minor between 1300 °C and 1500 °C compared to changing fO_2. Longer run times and higher temperatures result in a decrease in both ln*f*Cu and ln*f*Zn at a given logfO_2.

Experiments performed at lower oxygen fugacities are sparse and do not permit assessment of any temperature dependence. However, with decreasing fO_2, ln*f*Zn/ln*f*Cu increases from 2.09 ± 0.17 (N = 5) in pure CO_2 experiments (log fO_2 ≈ -3), 4.53 ± 0.86 (N = 3) at logfO_2 ≈ -5.5 and the single reliable point at logfO_2 -8 gives 5.30 (Fig. 2). The dependence of ln*f*Zn/ln*f*Cu with fO_2 stems from the stoichiometry of their respective vaporisation reactions. Copper is present as $CuO_{0.5}$ in silicate melts (i.e., monovalent) and Zn occurs in divalent form as ZnO. However, the stable gas species of both is the monatomic gas (that is, Cu^0 and Zn^0; Lamoreaux et al., 1987) and their vaporisation reactions from silicate melts are therefore written:

$$CuO_{0.5}(l) = Cu(g) + \frac{1}{4}O_2 \quad (4)$$

and, for Zn:

$$ZnO(l) = Zn(g) + \frac{1}{2}O_2 \quad (5)$$

The n = 1 reaction of Cu means that the vapour pressure of Cu(g), pCu, is proportional to $(fO_2)^{-1/4}$ whereas pZn depends on $(fO_2)^{-1/2}$. Therefore, lower oxygen fugacities will promote relatively more Zn vaporisation with respect to Cu, resulting in progressively higher ln$f$Zn/ln$f$Cu, proportional to $(fO_2)^{-1/4}$.

In detail, the degree of elemental loss of both Cu and Zn depends on the physical properties of the silicate melt sphere, the experimental run time and the effective equilibrium constant of the reaction (K*). To quantify the effects of these variables on elemental loss, we perform a non-linear least-squares minimisation to ln$f$(E) measured experimentally by varying K^* ($=K\gamma_{ev}\gamma_i$, where K is the equilibrium constant for reactions (4) and (5) in their standard states at T and 1 bar, γ_{ev} is the evaporation coefficient and γ_i is the activity coefficient of the melt oxide component) in the equation developed by Sossi et al. (2019):

$$\ln f(E) = \left(-\frac{K^*}{f(O_2)^{n/4}}\frac{3M}{r\rho}\sqrt{\frac{1}{2\pi M_i RT}}(t-t_0)\right). \quad (6)$$

Where n refers to the number of electrons exchanged in the vaporisation reaction (set equal to 1 for Cu and 2 for Zn; eqs. (4) and (5)). Other factors in the equation are known or controlled in each experiment; r the radius of the sphere, p its density, M and M_i are the molar mass of the sphere and of the evaporating species respectively, R the gas constant, T the absolute temperature, t the experimental run time and t_0 the time at which the element begins evaporating. This treatment invokes equilibrium only insofar as equations (4) and (5) are presumed to accurately describe the evaporation reactions occurring at the melt surface (as verified experimentally; Sossi et al., 2019), and the fO_2 of the melt is that imposed by the gas mixture. However, activity and evaporation coefficients of the evaporating species, as quantified by fits to the experimental data with the K* term, may deviate from unity, and hence from the equilibrium conditions of Knudsen evaporation (*e.g.,* Hoenig and Searcy, 1966).

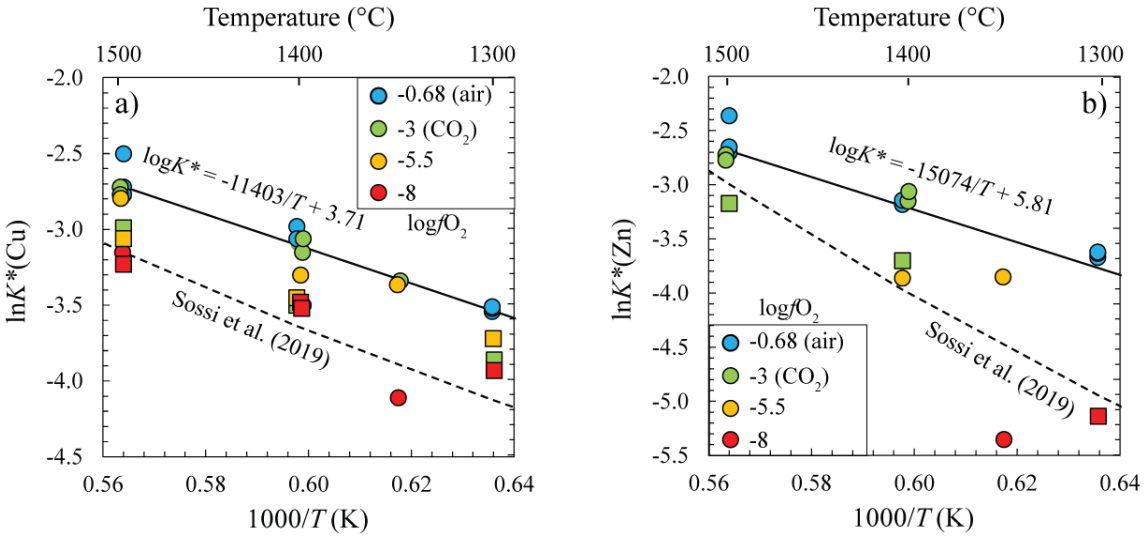

Figure 3. Fitted values of log$K$* expressed as a function of inverse temperature (1000/T) in Kelvin for **a)** Cu and **b)** Zn. Each point corresponds to a single experiment, where log$K$* is calculated by minimising the misfit to the measured ln$f$(E) using equation (6). The colour corresponds to a different oxygen fugacity, as in Fig. 2, while circles stand for the 'Cu-Zn' mixture and squares the 'Metalloids' mixture. The straight line fits are calculated from linear regressions to the data (T in K) for the 'Cu-Zn mix' (this work, solid line), excluding points at logfO_2 = -8 and -5.5 (for Zn) and logfO_2 -8 (for Cu), and to the data of Sossi et al. (2019) (dashed line).

The log$K$* of reaction for both Cu and Zn define a linear relationships with inverse temperature, expressed as 1000/T (Fig. 3), ranging from ~-3.5 at 1300 °C to ~-2.5 at 1500 °C, where an increase denotes that the vapour species is increasingly favoured (eqs. 4, 5). Compared with the log$K$* values in Sossi et al. (2019), in which silicate melts containing 1000 ppm Cu and Zn were evaporated, the log$K$* calculated herein is generally ~0.5 log units higher. This is also verified from measurements of the

306 'Metalloids' mixture (~1000 ppm) which plot near the Sossi et al. (2019) determination, suggesting this
307 difference is likely because $CuO_{0.5}$ and ZnO in the Cu-Zn melts (~20,000 ppm) are no longer in the
308 Henry's Law region, resulting in differences in their activity coefficients. Also evident is a systematic
309 decrease in log$K$* as a function of log$f$O$_2$ for both Cu (at log$f$O$_2$ -8) and Zn (at or below log$f$O$_2$ -5.5).
310 This attests to a decrease in the evaporation rate at that oxygen fugacity compared to that anticipated
311 from equation (6) with n = 1 for Cu and n = 2 for Zn, for which log$K$ should be independent of the fO$_2$.

312 *3.3. Copper and Zinc isotope ratios*

313 The starting material (SM) has δ^{65}Cu of +0.09 ± 0.02 ‰ (CuO, Alfa Aesar) relative to SRM-976 and
314 δ^{66}Zn = +0.16 ± 0.02 ‰ (ZnO, Alfa Aesar) relative to JMC-Lyon. All isotopic ratios are reported
315 relative to those of the starting materials ($\delta^{x}E_{SM}$), and are summarised in Table 1. Values of $\delta^{65}Cu_{SM}$
316 range from +0.11 ± 0.05 ‰ (run P07/04/17a) to +11.96 ± 0.09 ‰ (run P01/08/18d) and for $\delta^{66}Zn_{SM}$
317 vary between +0.30 ± 0.04 ‰ (run P07/04/17a) to +12.83 ± 0.01 ‰ (run 06/04/17c).

318 All experiments had sufficient quantities of Cu remaining in the glass to permit their isotopic analysis.
319 For Zn, however, higher temperature experiments (≥1400 °C) at reducing conditions (log$f$O$_2$ -5.5 and -
320 8) and longer run times (> 10 minutes) were poor in Zn. These samples, marked with an asterisk in
321 Table 1, deviate considerably from the ln$f$(E) *vs.* δ^{x}E trends defined by the other samples, indicative of
322 contamination by exchange with the furnace atmosphere (see *Supplementary Information*) and are not
323 discussed further. The slope in δ^{68}Zn *vs.* δ^{66}Zn space is 1.962±0.008 with an intercept of -0.032 ± 0.041
324 (N = 20). The value of the slope theoretically reflects the mass fractionation law governing isotope
325 fractionation, with an equilibrium process giving rise to a slope of 1.971 in δ^{68}Zn *vs.* δ^{66}Zn space
326 whereas purely kinetic fractionation yields 1.942. Following the approach of Young and Galy (2004)
327 and Wombacher et al. (2011), this dependence is better resolved in a plot of $\Delta^{68}Zn'_{(smp\text{-}eq)}$ *vs.* δ^{66}Zn (Fig.
328 4), where $\Delta^{68}Zn'_{(smp\text{-}eq)} = \delta^{68}Zn_{smp} - \delta^{66}Zn_{smp} \times 1.971$, and 'smp' denotes the measured value. Although
329 some samples appear to follow the kinetic trend defined for the masses or reduced masses of Zn in air
330 (1.951) or CO_2 (1.954), deviation from the equilibrium line shows no apparent dependence on the log$f$O$_2$
331 or temperature at which the sample equilibrated.

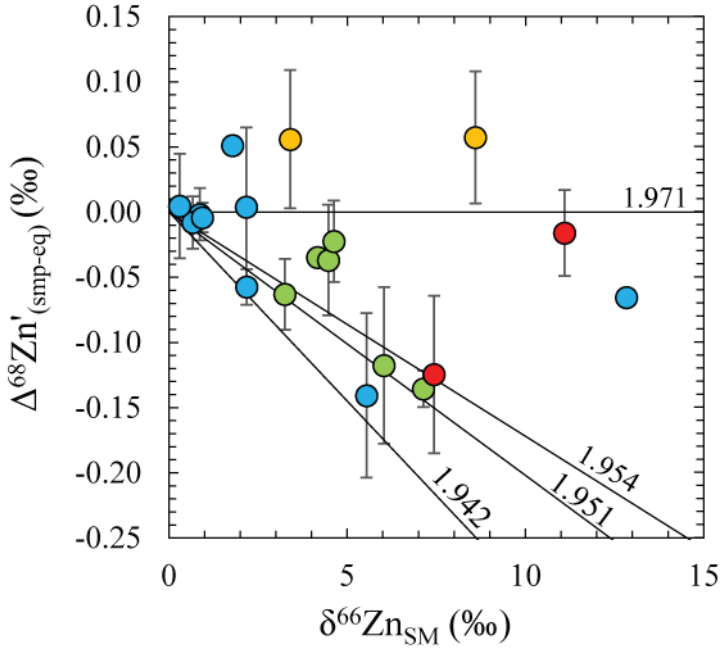

332

333 **Figure 4.** The $\Delta^{68}Zn'_{(smp\text{-}eq)}$ *vs.* $\delta^{66}Zn_{SM}$ of the experimental glasses. The slope of the line in $\delta^{68}Zn_{SM}$ *vs.* $\delta^{66}Zn_{SM}$
334 space is sensitive to the mode of isotopic fraction, in which, for the harmonic approximation, the kinetic and
335 equilibrium end-members define slopes of 1.971 (a horizontal line in this representation) and 1.942, respectively.
336 For kinetic transport in a diffusion-limited regime, the slope depends on the reduced masses, which gives 1.951

for ambient gas with the molar mass of air (0.029 kg/mol), and 1.954 in pure CO_2 (0.044 kg/mol). Colours denote the fO_2 of the experiment and are as per Fig. 1. Error bars are shown as 2SD.

For the isotopic evolution of a homogeneous and finite reservoir, the Rayleigh equation cast in terms of isotopic fractionation is written:

$$\frac{{}^{i}X^{t}_{E,liq}/\,{}^{j}X^{t}_{E,liq}}{{}^{i}X^{0}_{E,liq}/\,{}^{j}X^{0}_{E,liq}} = \frac{{}^{i/j}R^{t}_{E,liq}}{{}^{i/j}R^{0}_{E,liq}} = f_E^{\left({}^{i/j}E\alpha_{vap-liq}-1\right)}. \quad (7)$$

The fractionation factor may be calculated from measured data according to the approximation:

$${}^{i/j}E(\alpha_{vap-liq}) = \left(\left(\frac{\delta^{i/j}E_{liq}}{\ln f_E}\right)\frac{1}{10^3}\right) + 1. \quad (8)$$

Thus, the isotopic fractionation factor is determined by plotting δ^{65}Cu, δ^{66}Zn or δ^{68}Zn against ln*f*(Cu or Zn) (Fig. 5a, b).

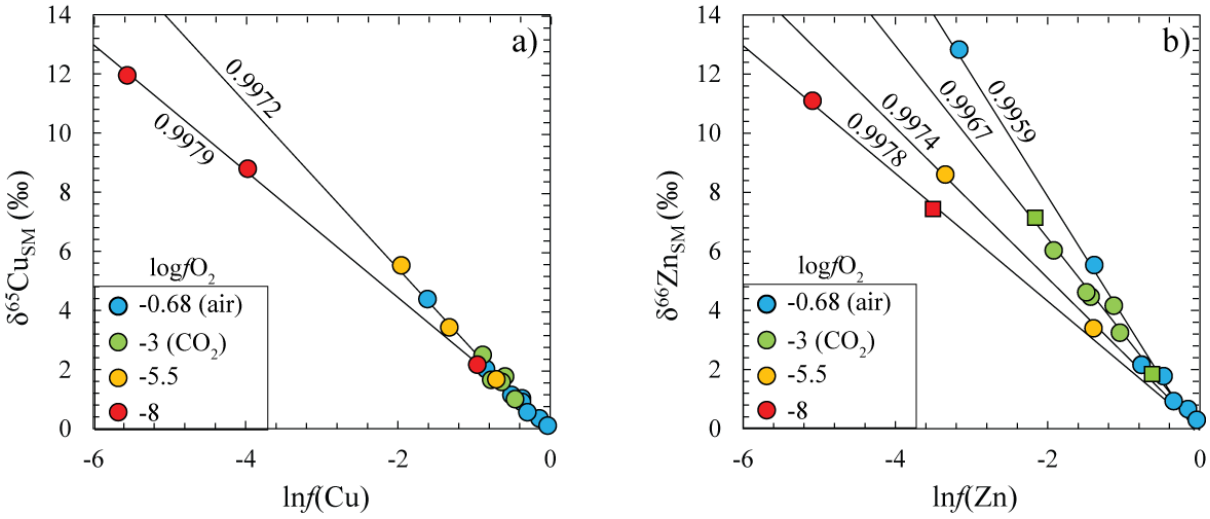

Figure 5. The isotopic composition of **a)** Cu, expressed as $\delta^{65}Cu_{SM}$ and **b)** Zn, expressed as $\delta^{66}Zn_{SM}$ (where 'SM' denotes the per mille deviation from the starting material), as a function of their respective relative abundances remaining in the glass, ln*f*(Cu) and ln*f*(Zn). Circles correspond to the 'Cu-Zn' mix, and squares to the 'metalloids' mix. The thin black lines are regressions through the data; for Cu, all data fall on a single line with a fractionation factor, $^{65/63}Cu(\alpha_{vap\text{-}liq}) = 0.9972$, save for the three samples equilibrated at logfO_2 = -8, which define $^{65/63}Cu(\alpha_{vap\text{-}liq}) = 0.9979$. For Zn, $^{66/64}Zn(\alpha_{vap\text{-}liq})$ decreases as a function of fO_2, from 0.9959 in air, 0.9967 at log$fO_2 \approx$ -3, 0.9974 at log$fO_2 \approx$ -5.5 and 0.9978 at logfO_2 = -8.

For Cu, there is no correlation between $^{65/63}Cu(\alpha_{vap\text{-}liq})$ and temperature or run duration. For $^{65/63}Cu(\alpha_{vap\text{-}liq})$ calculated for different fO_2 series (-0.68, -3, -5.5, -8), the three most oxidised series define the same fractionation factor, 0.9972 ± 0.0001 (N = 17) (Fig. 5a), whereas at logfO_2 -8 the fractionation factor is smaller, $^{65/63}Cu(\alpha_{vap\text{-}liq}) = 0.9979 \pm 0.0001$ (N = 3). Both series have intercepts ($\delta^{65}Cu_0$) very near 0; -0.18 ± 0.08 ‰ and +0.17 ± 0.21 ‰, respectively. For Zn, both Cu-Zn and Metalloids mixes give consistent values, with a difference in $^{66/64}Zn(\alpha_{vap\text{-}liq})$ observed at each logfO_2; 0.9959 ± 0.0002 (N = 8) at -0.68, 0.9967 ± 0.0002 (N = 7) at -3, 0.9974 (N = 2) at -5.5 and 0.9978 (N = 2) at -8 (Fig. 5b). At at logfO_2 = -0.68, $\delta^{66}Zn_0$ is -0.35 ± 0.23 ‰ while $\delta^{66}Zn_0$ = -0.07 ± 0.34 ‰ at logfO_2 = -3, whereas the two reducing series had their intercept forced through 0 due to the lack of points. Regressions not forced through the origin yield $^{66/64}Zn(\alpha_{vap\text{-}liq}) = 0.9973$ and 0.9977 at logfO_2 = -5.5 and -8, respectively.

4.0. Discussion

4.1. Diffusion and the effect of oxygen fugacity on elemental loss and the vapour-liquid fractionation factor

The observation that the apparent isotopic fractionation factors of Cu and Zn between liquid silicate and the gas phase decrease as a function of oxygen fugacity behoves an explanation. Over the range of fO_2 investigated, thermodynamic stability of the gas species for Cu and Zn should remain unchanged, with Cu^0 and Zn^0 predominating under all conditions (Lamoreaux et al., 1987; Sossi et al., 2019). Although Cu may also exist in its 2+ oxidation state in silicate melts at high oxygen fugacities (*e.g.*, in air), the observed shift in $^{65/63}Cu(\alpha_{vap\text{-}liq})$ occurs at $\log fO_2$ between -6 and -8; too reducing for Cu^{2+} to be stable (Holzheid and Lodders, 2001). On the other hand, Zn only exists as Zn^{2+} at all oxygen fugacities, meaning the systematic change in fractionation factor is not readily ascribed to a change in liquid or gas speciation as a function of fO_2.

The shift does coincide, however, with the appearance of zonation in both elements in the melts; for the experiment at $\log fO_2$ -8 and 1300 °C (26/12/18c) for Cu, and below $\log fO_2$ -6 for Zn (26/12/18a, b; Fig. 1). Formation of such a chemical and isotopic boundary layer at the evaporating surface may cause deviations of the fractionation factor between vapour – liquid inferred from the measurement of the bulk glass relative to cases in which the glass is homogeneous. The magnitude and sense of this isotopic divergence depend on the relative timescale of the element's evaporation rate *vs.* its homogenisation rate in the melt (which, for a sphere in the absence of a thermal gradient, can only occur by diffusion) and the difference in diffusion rates between the two isotopes in the melt (Young, 2000; Richter, 2004; Moynier et al., 2009).

Thus, if the vaporisation rate at the surface is known, the elemental zoning profiles, in conjunction with the observed $^{i/j}E(\alpha_{vap\text{-}liq})$, can be used to derive *i)* the elemental diffusion coefficient, *D* and *ii)* the relative differences in diffusion coefficients between two isotopes through the silicate melt. In order to do so, a central finite difference discretisation diffusion model in spherical co-ordinates (Crank, 1975; Ford-Versypt and Braatz, 2014) is implemented (*Appendix A1*). The model approximates the diffusion of an element or isotope through the silicate melt medium with a time-dependent boundary condition set by its evaporation at the surface of the bead.

The K^* value in eq. 6 is varied in order to produce the correct value of $X^t_{Cu,Zn}$ observed at the surface, taken to represent the steady-state value due to evaporation. Then, the value of D is varied in order to minimise the misfit to the objective function;

$$\chi^2 = \frac{\Sigma(X^t_{Cu,Zn,r}(obs) - X^t_{Cu,Zn,r}(calc))^2}{\Sigma\sigma(obs)} \quad (9)$$

Where χ^2 quantifies the sum of the misfit between the normalised concentration at each value of r (radial distance from the centre of the bead) that are observed (obs) and calculated by the model (calc) given the experimental run time, t. Results are shown in Table 2 and Fig. 6.

The fitted diffusion coefficient of Zn in ferrobasaltic melt is consistent among the three experiments, $1.56 \pm 0.25 \times 10^{-9}$ m^2/s at 1300 °C. There are no measurements of Zn diffusion coefficients in relevant compositions, however, tracer diffusivities of other divalent metal cations (Co^{2+}, Mn^{2+}) in basaltic melts are ~ 10^{-10} m^2/s (Lowry et al., 1982) at the same temperature. For Cu, the value of 2.61×10^{-9} m^2/s determined herein from a single experiment is nearly an order of magnitude higher than measured by Ni and Zhang (2016) in a basaltic melt at 1300 °C (~ 4×10^{-10} m^2/s). However, given the empirical dependence of $\log D$ on $1/\eta$ (*e.g.*, Mungall, 2002), and the factor of 10 lower viscosity of the melt composition used here, ~2.3 Pa.s, compared to the experimental basaltic melts of Lowry et al. (1982) and Ni and Zhang (2016), both ~ 27 Pa.s at 1300 °C, the values of D would be expected to be an order of magnitude higher.

Isotopic composition is predicted by constructing two finite difference profiles; one for each isotope. The fractionation factor between liquid and vapour at the boundary of sphere is modified by adjusting the ratio of the equilibrium constants of the isotope vaporisation reactions (K^*_i/K^*_j; eqs. A4 and A5) to yield the expected value of ${}^{i/j}E(\alpha_{vap\text{-}liq})_{surf}$ under conditions that are not diffusion-limited (*i.e.,* in air; 0.9959 for ${}^{66/64}Zn$, 0.9972 for ${}^{65/63}Cu$). Tracer diffusivity of two isotopes in a given medium is proportional to the inverse ratio of their masses, related by an exponent, β, i.e., $(M_j/M_i)^{\beta}$. Because the isotopic composition of the bulk sample is unknown, β cannot be determined independently, and must be assumed. By analogy with the diffusion of other divalent first-row transition metal cations in silicate melts, we adopt a value of $\beta = 0.015 \pm 0.010$ (Richter et al., 2009). This results in an isotopic fractionation factor due to diffusion, ${}^{i/j}E(\alpha_{diff})$ of 0.9998 ($\beta = 0.005$) to 0.9993 ($\beta = 0.025$).

Table 2. A summary of the experimental conditions of the 26/12/18a-c set of experiments (T = 1300 °C) measured for elemental zoning profiles, and the associated model parameters and results, assuming β = 0.015.

	26/12/18a	**26/12/18b**	**26/12/18c**	
$\log fO_2$	-6	-6	-8	
Time (mins)	10	20	5	
Element	Zn	Zn	Zn	Cu
D_0 (m^2/s)	$1.56(0.18) \times 10^{-9}$	$1.25(0.08) \times 10^{-9}$	$1.75(0.05) \times 10^{-9}$	$2.61(0.33) \times 10^{-9}$
f(Zn or Cu)$_{surf}$	0.46	0.13	0.05	0.25
f(Zn or Cu)$_{bulk}$	0.49	0.15	0.12	0.31
$\log K^*_{surf}$	-4.84	-4.73	-4.96	-3.30
$\log K^*_{bulk}$	-4.88	-4.76	-5.11	-3.37
t_{evap} (s)	1176	1379	316	435
$\delta^{66}Zn$ / $\delta^{65}Cu$ (‰) (calc)	2.93	7.88	6.85	3.16
${}^{i/j}E(\alpha_{vap\text{-}liq})_{surf}$ (assumed)	0.9959	0.9959	0.9959	0.9972
${}^{i/j}E(\alpha_{vap\text{-}liq})_{bulk}$ (calc)	0.9959	0.9959	0.9968	0.9973

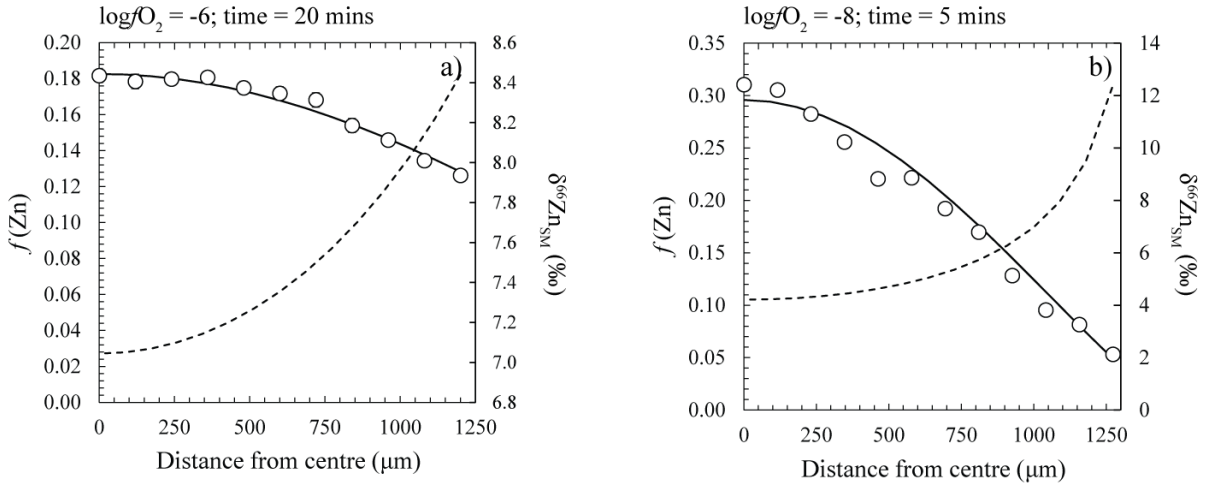

Figure 6. Laser-Ablation ICP-MS data for Zn abundances (white circles) as a function of core (0 μm) to rim (~1200 μm) in experimental glass spheres synthesised at 1300 °C; **a)** 26/12/18b, t = 20 mins, $\log fO_2$ = -6 and **b)** 26/12/18c, t = 5 mins, $\log fO_2$ = -8. Overlain on the data are, on the primary ordinate axis, the finite-difference model fit to the Zn abundances measured (solid black curve), and on the secondary ordinate axis, the modelled $\delta^{66}Zn_{SM}$ evolution with $\beta = 0.015$ as a function of radius (dashed black curve). The boundary condition is set by evaporative loss according to eq. (6) for both ${}^{66}Zn$ and ${}^{64}Zn$, with the constraint that vaporisation rates at the surface are ${}^{66/64}Zn(\alpha_{vap\text{-}liq}) = 0.9959$.

For $\beta = 0.015$, the isotopic composition of Zn (or Cu) in the centre of the bead is lighter than at the boundary, where ${}^{i/j}E(\alpha_{vap\text{-}liq})_{surf}$ is fixed (Fig. 6). This may seem counterintuitive, because the lighter isotope is able to diffuse more quickly than the heavier isotope, and therefore reaches the surface more rapidly. However, the key factor controlling whether the interior of the bead is isotopically heavy or light relative to the surface is the ratio of isotopic fractionation factor due to diffusion, ${}^{i/j}E(\alpha_{diff})$ to the

isotopic fractionation factor due to evaporation, ${}^{i/j}\mathrm{E}(\alpha_{vap\text{-}liq})$. Where ${}^{i/j}\mathrm{E}(\alpha_{diff}) > {}^{i/j}\mathrm{E}(\alpha_{vap\text{-}liq})_{surf}$, evaporation induces larger isotopic fractionation than can be compensated for by the faster diffusion of the lighter isotope relative to the heavier isotope, and the interior remains lighter than the rim, yet both are enriched relative to the initial composition. This causes the bulk ${}^{i/j}\mathrm{E}(\alpha_{vap\text{-}liq})_{bulk}$ value to increase (i.e., smaller fractionation) relative to that predicted by ${}^{i/j}\mathrm{E}(\alpha_{vap\text{-}liq})_{surf}$ (Table 2). However, as β increases such that ${}^{i/j}\mathrm{E}(\alpha_{diff}) < {}^{i/j}\mathrm{E}(\alpha_{vap\text{-}liq})_{surf}$, then ${}^{i/j}\mathrm{E}(\alpha_{vap\text{-}liq})_{bulk}$ is lower (i.e., larger fractionation factor) than ${}^{i/j}\mathrm{E}(\alpha_{vap\text{-}liq})_{surf}$, because the heavier isotope is unable to diffuse sufficiently rapidly to the surface, and becomes increasingly concentrated in interior of the bead. This phenomenon is illustrated graphically in *Fig. A1*.

At the constant value of β = 0.015 used to model the data, then, the degree to which ${}^{i/j}\mathrm{E}(\alpha_{vap\text{-}liq})_{bulk}$ increases (i.e., fractionation factor becomes closer to unity) relative to ${}^{i/j}\mathrm{E}(\alpha_{vap\text{-}liq})_{surf}$ is proportional to the timescale of evaporation relative to diffusion, denoted t_{diff}/t_{evap}. Experimental charges at log$f$O$_2$ -6 are predicted to show only little- to modest changes in ${}^{i/j}\mathrm{E}(\alpha_{vap\text{-}liq})_{bulk}$ compared to ${}^{i/j}\mathrm{E}(\alpha_{vap\text{-}liq})_{surf}$; as illustrated by the similar isotope composition of their interiors relative to the boundary layer (Fig. 6a). On the other hand, δ^{66}Zn is predicted to be lower by ~ 8 ‰ in the interior relative to the rim in the run at log$f$O$_2$ -8 (Fig. 6b), causing an increase in ${}^{i/j}\mathrm{E}(\alpha_{vap\text{-}liq})_{bulk}$ (0.9968) relative to ${}^{i/j}\mathrm{E}(\alpha_{vap\text{-}liq})_{surf}$ (0.9959). Given that the diffusion rate is near-constant with fO$_2$ (Table 2) and temperature is constant, this phenomenon arises due to the faster evaporation rate of Zn at low fO$_2$ (eq. 5). The characteristic evaporation timescale, t_{evap} (*i.e.*, the time taken to evaporate (1-f(E)$_{surf}$) relative to the experimental run time, t_{exp}), is given by:

$$t_{evap} = \frac{t_{exp}}{(1-f(E)_{surf})} \quad (10)$$

It is important to note that (1-f(E)$_{surf}$) is the fractional loss observed at the surface boundary layer, not that integrated throughout the entire bead. Whereas the diffusion timescale is given by (Crank, 1975):

$$t_{diff} = \frac{1}{2}\frac{r^2}{D} \quad (11)$$

With this in mind, t_{evap} is shown to be a factor of ~4 faster at log$f$O$_2$ = -8 than at log$f$O$_2$ = -6 (Table 2), giving rise to t_{diff}/t_{evap} of ~0.9 and ~0.28, respectively. The effect of t_{diff}/t_{evap} on ${}^{i/j}\mathrm{E}(\alpha_{vap\text{-}liq})_{bulk}$ follows a logistic function (Fig. 7), where, for β = 0.015:

$${}^{i/j}E\left(\alpha_{vap-liq}\right)_{bulk} = \frac{\left(1-{}^{\frac{i}{j}}E\left(\alpha_{vap-liq}\right)_{surf}\right)}{1+\exp\left(-3.85\left(\frac{t_{diff}}{t_{evap}}-1.24\right)\right)} + {}^{\frac{i}{j}}E\left(\alpha_{vap-liq}\right)_{surf} \quad (12)$$

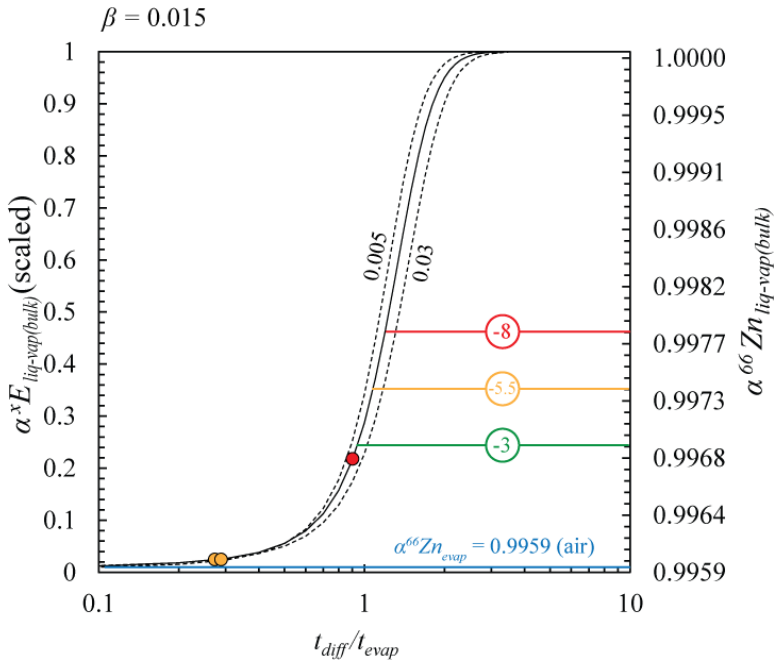

Figure 7. The dependence of $^{i/j}E(\alpha_{vap\text{-}liq})_{net}$ on the relative characteristic timescales of evaporation (t_{evap}) and diffusion (t_{diff}), assuming diffusion in the liquid is proportional to $(M_j/M_i)^{\beta}$, where $\beta = 0.015$ (solid line) and 0.005 and 0.030 (dashed lines). Model results (eq. 12) for the predicted $^{i/j}E(\alpha_{vap\text{-}liq})_{net}$ in experiments 26/12/18a-c (1300°C) are shown as yellow (logfO_2 -6) and red (logfO_2 -8) circles, assuming $^{i/j}E(\alpha_{vap\text{-}liq})_{surf} = 0.9959$. The measured $^{i/j}E(\alpha_{vap\text{-}liq})_{net}$ from other experimental runs at logfO_2s -0.68, -3, -5.5 and -8 (blue, green, yellow and red, respectively) are shown as horizontal lines.

The predicted increase in $^{i/j}E(\alpha_{vap\text{-}liq})_{net}$ falls short of that measured (Fig. 5) for a given fO_2, as shown by the horizontal lines on Fig. 7. Overlap between the red and yellow points with their respective coloured horizontal lines would constitute perfect agreement. However, given the uncertainties in the value of β and in the fractionation factor itself (especially considering the Cu and Zn isotope compositions of the zoned standalone samples were not determined), high t_{diff}/t_{evap} at lower fO_2 seems the most likely cause of increasing $^{i/j}E(\alpha_{vap\text{-}liq})_{net}$ observed.

4.2. A general law for vaporisation

The Hertz-Knudsen-Langmuir (HKL) equation provides a quantitative means of assessing the mechanisms of elemental and isotopic fractionation due to evaporation that are observed experimentally. The degree to which gas molecules evaporating at the surface of a melt sphere equilibrate with the melt depends on the rate with which they are transported away from the surface, relative to the rate at which they are produced, a relationship described numerically;

$$\left(\frac{dn_i}{dt}\right)_{net} = -4\pi r^2 \frac{\gamma_{ev} p_{i,eq} - \gamma_{cn} p_{i,s}}{\sqrt{2\pi R M_i T}}. \quad (13)$$

Equation (13) states that the molar rate at which a species, i, in an ideal gas with a Maxwell-Boltzmann distribution of kinetic energies impinges upon a spherical surface is proportional to difference between the equilibrium partial pressure of that species ($p_{i,eq}$) and its actual pressure at the boundary layer of the evaporating surface, $p_{i,s}$, multiplied by their evaporation (γ_{ev}) and condensation (γ_{cn}) coefficients, respectively. Although the value of $p_{i,s}$ is not readily measured (*e.g.* by a probe that would itself perturb the boundary layer), it can be estimated by considering that, in a system with finite quantity of i, the net

production of gaseous molecules at the evaporating surface and their molar removal rate (mol/s) by mass transport must be equal, *i.e.*, $\left(\frac{dn_i}{dt}\right)_{net} = \left(\frac{dn_i}{dt}\right)_{trans}$, where $\left(\frac{dn_i}{dt}\right)_{trans}$ is given by (Bartlett, 1967):

$$\left(\frac{dn_i}{dt}\right)_{trans} = -4\pi r^2 k_c \frac{(\gamma_{cn} p_{i,s} - p_{i,\infty})}{P}(1 - \exp(\xi)\mathrm{erfc}\sqrt{\xi}), \quad (14)$$

Here, $\xi = \frac{D_{ik}t}{2r^2}$, where D_{ik} the diffusion rate of species i through the gas otherwise composed of molecules with an average molar mass of k, r is the radius of the sphere, designates the approach to steady state conditions, which, in our experiments occurs after ~5 s (ξ > 500). At steady state, the mass transport rate is thus proportional to the partial pressure difference between $p_{i,s}$ and $p_{i,\infty}$ at an infinite distance from the boundary layer (taken here to be 0), related by the reciprocal total pressure (P) and the mass transfer coefficient, k_c. This quantity, which has units of mol/m^2.s, describes the facility with which mass is transported within a given medium, in this case, a flowing gas, and hence determines the thickness of the boundary layer surrounding the melt droplet.

The mass transfer coefficient is estimated through empirical correlations between dimensionless numbers determined under experimental conditions, and, for gases, is generally proportional to the diffusion rate raised to the power of 2/3 (Fuchs, 1959; Cussler, 2009). Expressions for k_c vary depending on whether the medium through which mass transfer occurs is subject to forced- or natural convection. The threshold between the two regimes is given by the ratio of the Grashof number[1] to the Reynolds number[2] squared, where values >> 1 indicate natural convection, and those << 1 reflect forced convection. For forced convection, Frössling (1938) derived the following expression:

$$k_c = \left(\frac{P}{RT}\right)\frac{D_{ik}}{r}\left(2 + 0.6Re^{\frac{1}{2}}Sc^{\frac{1}{3}}\right), \quad (15)$$

Where *Re* is the Reynolds number and *Sc* is the Schmidt number[3]. Under natural convection conditions or for laminar flow (Gr/Re^2 >> 1), as is the case for our experimental set-up (*Appendix B1*), the Chilton-Colburn equation (Chilton and Colburn, 1934; Wimber et al., 1977; Liu and Bautista, 1981), is suitable for calculating k_c:

$$k_c = \frac{hP}{RT\rho C_P}\left(\frac{C_P \rho D_{ik}}{\kappa}\right)^{\frac{2}{3}}, \quad (16a)$$

$$k_c = \left(\frac{P}{RT}\right)\frac{(D_{ik})^{\frac{2}{3}}}{r}\left((\frac{\kappa}{\rho C_P})^{\frac{1}{3}} + 0.3(U_\infty L)^{\frac{1}{2}}\left(\frac{\rho}{\eta}\right)^{\frac{1}{6}}\right) \quad (16b)$$

Where h is the heat transfer coefficient, U_∞ is velocity of the flowing gas at an infinite distance from the sample, L is the diameter of the tube, ρ is the density of the gas, η its viscosity, κ its thermal conductivity. Values and units for each term, and their meaning, are described in *Appendix B1*. The value of k_c is evaluated for the conditions of the furnace, at 1 bar both by direct measurement of h, 90 W/m^{2}K (Sossi et al. 2019) with eq. 16a, and by eq. 16b from the gas flow rate (0.025 m/s) and tube diameter (0.042 m), for which k_c values of 12.4 and 13.3 mol/m^2.s are obtained, respectively.

Recent studies (Richter et al., 2002; Young et al., 2019), have approximated k_c by assuming transport occurs purely by binary diffusion, and hence, in their analysis $k_c = \frac{D_{ik}P}{rRT}$, see also Craig (1968). Although our expression has a similar form, it differs in two principal ways; 1) it accounts for the advection and convection of the gas in the vicinity of the sample in accelerating mass transport (Stefan

[1] Grashof number, $Gr = g\rho^2\beta\Delta TL^3/\eta^2$, where g is the acceleration due to gravity, β is the coefficient of thermal expansion ($1/T$ for an ideal gas) and ΔT is the temperature difference between the sample surface and bulk gas.
[2] Reynolds number, $Re = U_\infty\rho L/\eta$.
[3] Schmidt number, $Sc = \eta/D_{ik}\rho$.

flow) and 2) k_c is proportional to $(D_{ik})^{\frac{2}{3}}$ at the diffusive limit (where D_{ik} is small) and not D_{ik}. Under forced convection, the dependence of k_c on D_{ik} varies as a function of the Schmidt number, from a proportionality with $(D_{ik})^{\frac{2}{3}}$ at low *Sc* to one with D_{ik} at high *Sc* (eq. 15). The k_c calculated herein for natural convection is ~3 times faster than the diffusion-only value, ~3.8 mol/m^2.s.

Equating eq. (13) with eq. (14), and re-arranging, the unknown $p_{i,s}$ term is eliminated to obtain:

$$\left(\frac{dn_i}{dt}\right)_{net} = -4\pi r^2 \frac{\frac{\gamma_{i,ev} p_{i,eq}}{\sqrt{2\pi R M_i T}}}{1+\frac{\gamma_{i,cn} P}{k_c \sqrt{2\pi R M_i T}}(1-\exp(\xi)\mathrm{erfc}\sqrt{\xi}),} \quad (17)$$

As such, when mass transport is fast (*i.e.*, k_c is large), the denominator in eq. (17) tends to 1, and the net evaporation rate approaches the maximum evaporation rate ($p_{i,s}$ = 0), given by the numerator. The value of $p_{i,eq}$ for any melt oxide species, $M^{x+n}O_{\frac{x+n}{2}}$, is given by its congruent evaporation:

$$M^{x+n}O_{\frac{x+n}{2}}(l) = M^{x}O_{\frac{x}{2}}(g) + \frac{n}{4}O_2(g) \quad (18)$$

where the equilibrium partial pressure of the stable gas species, $M^{x}O_{\frac{x}{2}}$, at the surface is:

$$p_{i,eq} = p\left(M^{x}O_{\frac{x}{2}}\right) = \frac{K_{(r)} X\left(M^{x+n}O_{\frac{x+n}{2}}\right)\gamma\left(M^{x+n}O_{\frac{x+n}{2}}\right)}{f(O_2)^{\frac{n}{4}}} \quad (19)$$

Where X is the mole fraction and γ the activity coefficient of $M^{x+n}O_{\frac{x+n}{2}}$ in the melt. Integrating with respect to time and concentration, following Sossi et al. (2019) (see their equations (2) to (8) for derivation), gives the analytical form of the equation:

$$\frac{X_i^t}{X_i^0} = \exp\left(-\frac{\frac{K^*_{(r)}}{f(O_2)^{n/4}}\frac{3M}{r\rho}\sqrt{\frac{1}{2\pi M_i RT}}(t-t_0)}{1+\frac{\gamma_{i,cn}\rho C_P}{h}\left(\frac{\kappa}{C_P \rho D_{ik}}\right)^{\frac{2}{3}}\sqrt{\frac{RT}{2\pi M_i}}(1-\exp(\xi)\mathrm{erfc}\sqrt{\xi}),}\right) \quad (20)$$

Where $K^*_{(r)} = K_{(r)}\gamma\left(M^{x+n}O_{\frac{x+n}{2}}\right)\gamma_{i,ev}$. Evaluating the denominator with k_c calculated from eq. (16) for evaporation at 1 bar yields ~ 100 (dimensionless), which results in a flux that is therefore ~ 10^2 × lower (*cf. eq.* 17*)* than for evaporation into a vacuum (for which the denominator is equal to unity), all else being equal. This factor was determined empirically when calculating *K** values in Sossi et al. (2019) and is predicted from first-principles herein.

Importantly, k_c is nearly independent of which element is being investigated, as it is determined primarily by the properties of the fluid medium surrounding the sample, and only mildly by those of the evaporating species themselves, *via* the D_{ik} term (*cf. eqs.* 15, 16). Furthermore, k_c does not change significantly as a function of fO_2, nor for different gas flow rates (provided flow remains laminar). This expectation is confirmed in tests with two different flow rates at 1500 °C (P31/07/18a and b; 200 ml/min and 20 ml/min, respectively) and 1400 °C (P01/08/18a and b; 200 ml/min and 20 ml/min, respectively) each using pure CO_2, in which the fractional vapour loss was within uncertainty of unity (Table 1). The same is true of samples run in air compared to those run in a flowing gas, k_c varies from 13.3 mol/m^2.s with U = 0.025 m/s to 11.1 mol/m^2.s with no gas flow.

Compared with elemental loss, predicting isotopic fractionation is comparatively simpler, because the global variables cancel when taking the ratio of fluxes of two isotopes. Isotopic fractionation is calculated as:

$$^{i/j}E\left(\alpha_{vap-liq}\right)_{net} = -4\pi r^2 \frac{\frac{\gamma_{i,ev}p_{i,eq}}{\sqrt{2\pi RM_iT}}}{1+\frac{\gamma_{i,cn}P}{k_{c,i}\sqrt{2\pi RM_iT}}(1-\exp(\xi)\mathrm{erfc}\sqrt{\xi})} \Big/ -4\pi r^2 \frac{\frac{\gamma_{j,ev}p_{j,eq}}{\sqrt{2\pi RM_jT}}}{1+\frac{\gamma_{j,cn}P}{k_{c,j}\sqrt{2\pi RM_jT}}(1-\exp(\xi)\mathrm{erfc}\sqrt{\xi})} \quad (21)$$

This equation can be simplified considering that the denominator is related to the ratio of $p_{i,s}$ and $p_{i,eq}$ by equations (13) and (14) and simplifying:

$$1 - \frac{1}{1+\frac{\gamma_{i,cn}P}{k_c\sqrt{2\pi RMT}}(1-\exp(\xi)\mathrm{erfc}\sqrt{\xi})} = \left(\frac{p_{i,s}}{p_{i,eq}}\right) \quad (22)$$

Therefore, simplifying eq. (21) and substituting in eq. (22), one obtains:

$$^{i/j}E\left(\alpha_{vap-liq}\right)_{net} = \frac{\gamma_{i,ev}p_{i,eq}}{\gamma_{j,ev}p_{j,eq}}\sqrt{\frac{M_j}{M_i}}\frac{\left(1+\frac{\gamma_{j,cn}P}{k_{c,j}\sqrt{2\pi RM_jT}}\right)}{\left(1+\frac{\gamma_{i,cn}P}{k_{c,i}\sqrt{2\pi RM_iT}}\right)} = \frac{\gamma_{i,ev}p_{i,eq}}{\gamma_{j,ev}p_{j,eq}}\sqrt{\frac{M_j}{M_i}}\frac{\left(1-\frac{p_{i,s}}{p_{i,eq}}\right)}{\left(1-\frac{p_{j,s}}{p_{j,eq}}\right)} \quad (23)$$

Which is applicable to evaporation in a steady-state, open system for any pressure and gas flow regime. When transport is sufficiently fast that $p_{i,s}/p_{i,eq} \rightarrow 0$, then $^{i/j}E(\alpha_{vap-liq})_{net} \rightarrow (M_j/M_i)^{0.5}$. The inverse case occurs when transport is slow relative to evaporation such that $p_{i,s}/p_{i,eq} \rightarrow 1$. Thus, when taking the ratio of the fluxes of two isotopes (eq. 21), all terms become small with respect to $1/k_c$ to give:

$$^{\frac{i}{j}}E\left(\alpha_{vap-liq}\right)_{net}(D_{ik} \rightarrow 0) = \frac{\frac{\gamma_{j,cn}\rho C_P}{h}\left(\frac{\kappa}{C_P\rho D_{jk}}\right)^{\frac{2}{3}}}{\frac{\gamma_{i,cn}\rho C_P}{h}\left(\frac{\kappa}{C_P\rho D_{ik}}\right)^{\frac{2}{3}}} = \frac{\gamma_{j,cn}}{\gamma_{i,cn}}\left(\frac{D_{ik}}{D_{jk}}\right)^{\frac{2}{3}} = \frac{\gamma_{i,cn}}{\gamma_{j,cn}}\left(\frac{\mu_{jk}}{\mu_{ik}}\right)^{\frac{1}{3}} \quad (24)$$

Where $\mu_{ik} = \frac{m_i m_k}{m_i+m_k}$, the reduced mass of i and k. Since, save for D_{ik}, all terms that determine k_c are properties of the gas phase in which evaporation occurs (*i.e.,* they are independent of isotopic mass) they also cancel. This assumption holds provided the evaporating species are dilute enough that they do not themselves influence the properties of the gas medium k. Then, because D_{ik} is itself proportional to the inverse square root of the reduced mass $(\mu_{ik})^{-\frac{1}{2}}$ (eq. B6), $^{i/j}E(\alpha_{vap-liq})_{net}$ is proportional to $(\mu_{jk}/\mu_{ik})^{1/3}$ at the diffusive limit (*i.e.*, when diffusion through the gas is the rate-limiting step for mass transfer of the evaporating species away from the evaporating surface).

At the high-temperatures relevant to these experiments, quantum contributions (*e.g.* vibrational frequency) to the free energy change of the isotopic substitution are insignificant relative to the thermal energy of the system (3/2 k_BT, k_B = Boltzmann's constant) such that they can be ignored. Thus, we make the assumption that $p_{i,eq} = p_{j,eq}$. Similarly, we assume that both the evaporation and condensation coefficients are unity for liquids (see Sossi and Fegley, 2018 and Shornikov, 2015 for discussions). Evaluating the denominator of the left-hand side of eq. (22) for evaporation experiments at 1 bar (~ 100), one finds that $p_{i,s}/p_{i,eq} \approx 0.99$. In detail, this value varies according to the molar mass of the evaporating species, because k_c and M depend on the precise mass of the isotope considered. Thus, using eq. (22), the values of $\frac{p_{i,s}}{p_{i,eq}}$ and $\frac{p_{j,s}}{p_{j,eq}}$ obtained for the mass pairs ^{65}Cu-^{63}Cu and ^{66}Zn-^{64}Zn, (where i = ^{66}Zn or ^{65}Cu and j = ^{64}Zn or ^{63}Cu) are substituted into eq. (23) and show that $^{i/j}E(\alpha_{vap-liq})_{net}$ approaches $(D_{ik}/D_{jk})^{2/3}$, the diffusive limit (as D_{ik} tends to 0), which is 0.9966 in air or 0.9958 in pure CO_2 for both $^{66/64}$Zn and $^{65/63}$Cu. These calculations overlap with the values observed in samples for which elemental zoning in the condensed phase is absent (as informed from analogue experiments, Sossi et al., 2019); 0.9959 ± 0.0002 for $^{66/64}$Zn and 0.9972 ± 0.0001 for $^{65/63}$Cu.

For Cu, whether the experiments were performed in air or CO-CO_2 mixtures, the isotopic fractionation factor remains constant, whereas eq. 24 would predict a decrease in $^{i/j}E(\alpha_{vap-liq})$ (*i.e.*, more fractionation) as the molar mass of the gas phase increases from air (0.029 kg/mol) to CO_2 (0.044 kg/mol). We also

note that slight deviations from unity are permitted for $\frac{\gamma_{i,ev}}{\gamma_{j,ev}}$ and $\frac{p_{i,eq}}{p_{j,eq}}$. For a monatomic gas, $\frac{p_{i,eq}}{p_{j,eq}}$ must be < 1, as the heavier isotope (*i*) will have a slightly lower equilibrium partial pressure than the lighter isotope (*j*). The same is true for $\frac{\gamma_{i,ev}}{\gamma_{j,ev}}$ because the value of $\gamma_{i,ev}$ relates to vibrational frequencies (Knacke and Stranski, 1952; Penner, 1952; Ackermann et al., 1962) making it difficult to envisage any kinetic mechanism that would favour detachment of the heavier isotope over the lighter isotope of the same chemical species. Both processes will decrease ${}^{i/j}\mathrm{E}(\alpha_{liq\text{-}vap})$ (more fractionation) compared to those calculated from eq. 23 assuming $\frac{\gamma_{i,ev}p_{i,eq}}{\gamma_{j,ev}p_{j,eq}} = 1$. For example, given ${}^{66/64}\alpha_{\mathrm{Zn(g)\text{-}ZnO(s)}} = \frac{p_{66,eq}}{p_{64,eq}} = 0.99985$ from Ducher et al. (2016) at 1573 K, a value of $\frac{\gamma_{66,ev}}{\gamma_{64,ev}} = 0.9995$ would be required to give ${}^{66/64}\mathrm{Zn}(\alpha_{vap\text{-}liq}) = 0.9959$. However, given the complexity of predicting the value of k_c in real systems together with possible small variations in $\frac{\gamma_{i,ev}}{\gamma_{j,ev}}$ and $\frac{p_{i,eq}}{p_{j,eq}}$ and in the experimental conditions, we consider that the experimental values are satisfactorily reproduced by the model. It therefore also illustrates that the assumption of the ratios of evaporation coefficients of two isotopes of a given species being equal to unity is well-founded.

5.0. Implications

5.1. Comparison with experimental data

Although vaporisation studies have typically sought to explain the cosmochemical features of Calcium-Aluminium-rich Inclusions (CAIs) or chondrules, and have thus been performed at very low pressure (vacuum) conditions (Wang et al., 2001; Richter et al., 2002; Yu et al., 2003; Janney et al., 2004; Wombacher et al., 2004; Dauphas et al., 2004; Richter et al., 2007; Knight et al., 2009; Mendybaev et al., 2017), an increasing number of studies have turned to volatilisation experiments at 1 bar (Yu et al., 2003; Richter et al., 2011; Wimpenny et al., 2019) in order to understand the origin of the limited isotopic fractionation observed in planetary materials.

The formalism developed in section *4.2.* permits enumeration of the effect of total pressure on the vapour-liquid fractionation factor. Higher total pressures cause a linear decrease in both the diffusion coefficient, D_{ik} (eq. B6) and in the density of the ambient gas (eq. B2). The net effect is to decrease the mean free path of evaporating molecules, thereby depressing the evaporation rate indirectly through the build-up of molecules (higher $\frac{p_{i,s}}{p_{i,eq}}$) in the gaseous boundary layer surrounding the melt sphere. Because the mass transfer coefficient, k_c, is proportional to $(D_{ik})^{\frac{2}{3}}$, which is itself proportional to $1/P$, and $\rho^{-1/3}$, which is itself proportional to P (*cf.* eq. 16), k_c varies with $1/P$. This dependence mirrors that predicted from the diffusion-only mass transfer coefficient, for which k_c is proportional to D_{ik} (*e.g.,* Richter et al., 2002).

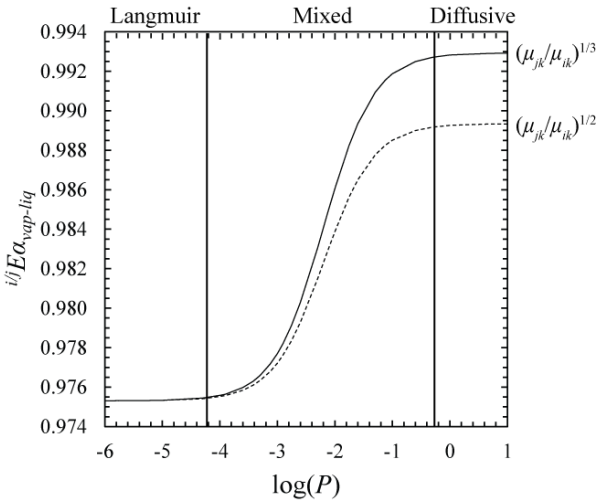

Figure 8. The effect of pressure, expressed as log(P) (with P in bars) on the vapour-liquid isotopic fractionation factor, $^{i/j}E(\alpha_{vap\text{-}liq})_{net}$. Here, $i = {}^{41}K$ and $j = {}^{39}K$, and the mass transfer coefficient is calculated at 1450 °C for natural convection in air (k), M_k = 0.029 kg/mol. The fractionation factor is then calculated according to the dependence on $(D_{ik}/D_{jk})^{2/3}$ (solid line) and (D_{ik}/D_{jk}) (dashed line), where the value of the mass transfer coefficient is otherwise constant. Solid vertical lines delineate the fields of Langmuir evaporation ($p_{i,s}/p_{i,eq} < 0.01$) and the diffusion-limited regime ($p_{i,s}/p_{i,eq} > 0.99$) with the intervening pressure range giving rise to a 'mixed' evaporative regime. Lighter ambient gases (k) will shift these curves to the left and to a higher diffusion-limited ceiling, and vice-versa.

Calculation of $^{41}K/^{39}K(\alpha_{vap\text{-}liq})_{net}$ from 10 bar to 10^{-6} bar at 1450 °C for a gas with mean molar mass of 0.029 kg/mol indicates that the diffusive limit (defined as $p_{i,s}/p_{i,eq} > 0.99$) occurs above ~0.5 bar, whereas pure Langmuir vaporisation (when $p_{i,s}/p_{i,eq} < 0.01$) is expected below ~10^{-4} bar (Fig. 8). High-precision evaporation experiments over a range of pressures are required in order to verify these predictions. Note that, because this treatment assumes steady-state loss (*cf.* eq. 14), the fractionation factor tends to the diffusion-limited value (~0.993 in air for $^{41/39}K$), rather than to the equilibrium fractionation factor (~ 1). The latter would be applicable as an upper limit to cases in which the gas remains in contact with the condensed phase (*i.e.,* a closed system) at any pressure.

At the diffusive limit, as is relevant for evaporation at 1 bar, our expression predicts a fractionation factor that is proportional to $(\mu_{jk}/\mu_{ik})^{1/3}$ (eq. 24). However, because Richter et al. (2002) and Young et al. (2019) assume that k_c depends simply on D_{ik}, these studies predicted that $^{i/j}E(\alpha_{vap\text{-}liq})_{net}$ tends to $(\mu_{jk}/\mu_{ik})^{1/2}$. To ground-truth these different dependencies, we summarise existing experimental data for the isotope fractionation of moderately volatile elements during their vaporisation from silicate melts at 1 bar in Table 3 and Fig. 9. These experiments were all performed under low flow rates that permits application of eq. (16) in the limit D_{ik} tends to 0. Increasingly higher flow rates would accelerate mass transfer, with the net effect of decreasing $p_{i,s}/p_{i,eq}$, and thus $^{i/j}E(\alpha_{vap\text{-}liq})_{net}$ (*i.e.,* more fractionation) relative to the $p_{i,s}/p_{i,eq}$ = 1 limit.

Table 3. Isotopic fractionation of moderately volatile elements during their evaporation from silicate melts at a total pressure of 1 bar.

Element	Isotope Ratio	Gas medium	log$f$O$_2$	Temperature (° C)	Material	$^{i/j}E(\alpha_{vap\text{-}liq})$ Diffusion only	$^{i/j}E(\alpha_{vap\text{-}liq})$ This work	$^{i/j}E(\alpha_{vap\text{-}liq})$ Observed	Ref.
K	41/39	Air	-0.68	1450	IIAB Chondrule	0.9890	0.9925	0.9917 ± 0.0015	Y+'03
K	41/39	CO_2-H_2	-6.93	1430	IIAB Chondrule	0.9891	0.9927	0.9935 ± 0.0006	R+'11
K	41/39	H_2	-	1450	IIAB Chondrule (K-rich, Fe-free)	0.9987	0.9990	0.9993 ± 0.0004	R+'11

K	41/39	He	-	1450	IIAB Chondrule (K-rich, Fe-free)	0.9977	0.9983	0.9984 ± 0.0003	R+'11
Zn	66/64	Ar	-	1600 - 2200	Arkosic soil	0.9942	0.9960	0.9996 ± 0.0003	W+'19
Zn	66/64	Ar	-	1600 - 2200	Rhyolitic soil	0.9942	0.9960	0.9981 ± 0.0003	W+'19
This work									
Cu	65/63	Air, CO_2	-0.68, -3, -5.5	1300 - 1500	Ferrobasalt	0.9950	0.9966	0.9972 ± 0.0001	
Zn	66/64	Air	-0.68	1300 - 1500	Ferrobasalt	0.9951	0.9966	0.9959 ± 0.0002	

Y+'03 = Yu et al. (2003); R+'11 = Richter et al. (2011); W+'19 = Wimpenny et al. (2019)

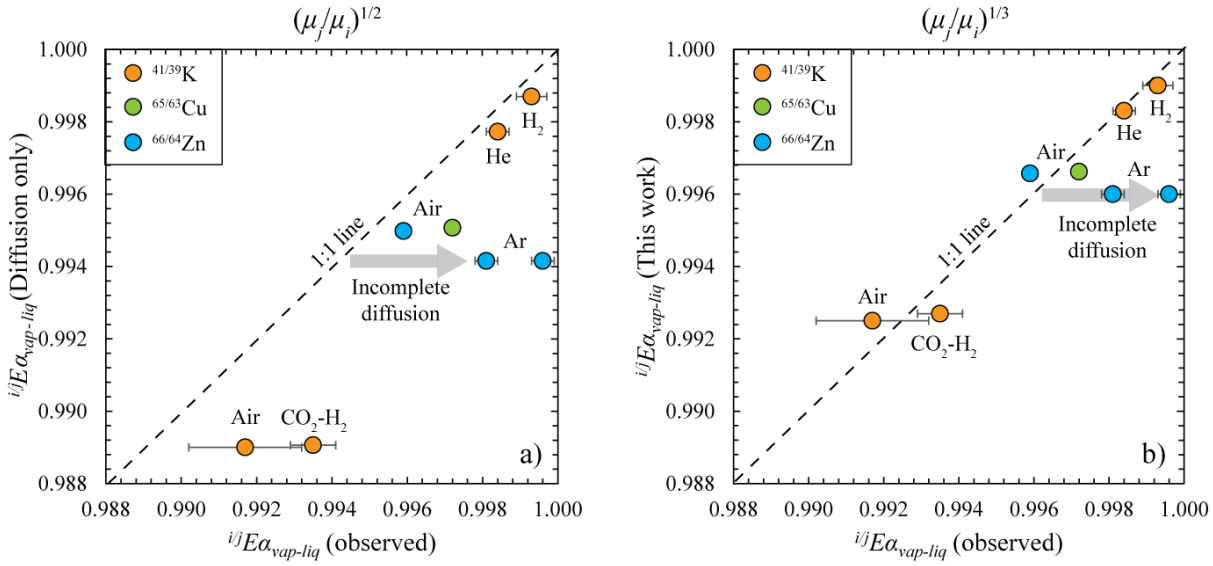

Figure 9. A comparison between the isotopic fractionation factor between vapour and liquid, $^{i/j}E(\alpha_{vap\text{-}liq})_{net}$, observed in experimental studies of the evaporation of $^{41/39}$K (orange), $^{65/63}$Cu (green) and $^{66/64}$Zn (blue) from silicate melts at 1 bar and a variety of gas mixtures (labelled next to points), compared to that predicted according to **a)** a $(\mu_{jk}/\mu_{ik})^{1/2}$ dependence and **b)** a $(\mu_{jk}/\mu_{ik})^{1/3}$ dependence on mass transport through the gas phase. The dashed 1:1 line denotes perfect agreement between experiment and theory.

Although both expressions correctly predict the sense of isotopic fractionation, expressions with a $(\mu_{jk}/\mu_{ik})^{1/2}$ dependence underestimate the value of $^{i/j}E(\alpha_{vap\text{-}liq})_{net}$ (Fig. 9a), whereas the $(\mu_{jk}/\mu_{ik})^{1/3}$ proportionality derived herein (*Appendix B1*) lies within ± 0.0005 of the experimental data (Fig. 9b). Experiments over a wide range of gas mixtures and isotopic systems therefore empirically verify the dependence on $(\mu_{jk}/\mu_{ik})^{1/3}$. This new formalism also ameliorates the difficulty of having to account for fractionation factors that are smaller (i.e., higher $^{i/j}E(\alpha_{vap\text{-}liq})_{net}$) than predicted by the $(\mu_{jk}/\mu_{ik})^{1/2}$ dependence, as is the case for almost all isotopic systems investigated (Fig. 9a). Values of $^{i/j}E(\alpha_{vap\text{-}liq})_{net}$ that exceed the diffusion-limited value require either that *i)* $p_{i,eq} > p_{j,eq}$ and/or *ii)* $\gamma_{i,ev} > \gamma_{j,ev}$; both of which are equally unphysical (*section 4.2.*). The departure to higher values of $^{i/j}E(\alpha_{vap\text{-}liq})_{net}$ observed in some vacuum experiments (particularly for $^{25/24}$Mg; Richter et al. 2007; Mendybaev et al. 2017) may relate to different evaporation coefficients among *different species*. That is, that $\gamma MgO/\gamma Mg > 1$, such that there is more MgO(g) relative to Mg(g) than expected under equilibrium conditions, meaning the mean molar mass of Mg in the gas phase increases. A detailed exploration of such a hypothesis is beyond the scope of this work.

Conspicuous in Fig. 9 are the $^{66/64}Zn(\alpha_{vap\text{-}liq})$ fractionation factors of Wimpenny et al. (2019), which fall to slightly (rhyolitic soil) or significantly (arkosic soil) higher values. Notably, the experimental charges at temperatures below 1800 °C were not fully molten, as attested to by their non-aerodynamic forms, making it difficult to quantify evaporation rates thermodynamically. Moreover, all other variables being

held constant, the amount of Zn remaining in the melt does not decrease as a function of time (for runs < 60 s) as would be expected from eq. 6. This suggests evaporation did not reach a steady state until ~ 60 s. Indeed, arkosic soil shows a variation of $^{66/64}Zn(\alpha_{vap\text{-}liq})$ with run time. After 60 s, the vaporisation rate can be modelled with a $\log K^*_{Zn}$ value of -3.75 ± 0.29 at all temperatures for both the arkosic and rhyolitic soil, which is lower (slower evaporation rate) than predicted from extrapolation of the trends shown in Fig. 3. The rhyolitic soil shows no dependence of $^{66/64}Zn(\alpha_{vap\text{-}liq})$ on experimental run time, and is also much closer to the predicted value in pure Ar, 0.9960.

Because both compositions have > 70% SiO_2 by definition (and likely >90% in the case of arkose) and the experiments were performed at 1 bar where water solubility is low (< 0.1 wt. %; Dixon et al., 1995), the melt viscosity in both cases is likely to be of the order of $\log\eta \approx 3$ to 4 at 2000 °C (Stevenson et al., 1998; Giordano et al., 2008); at least 10^3 × more viscous than the melt compositions used herein, meaning diffusion rates of Zn were also 10^3 × slower. A quantitative model of vaporisation rate for the experiments of Wimpenny et al. (2019) cannot be constructed because they were not fO_2-buffered, nor were zoning profiles across the glass beads measured. However, the empirical observation that $^{66/64}Zn(\alpha_{vap\text{-}liq})$ in their experiments are higher than *i)* predicted for a diffusive-limited gas regime (Fig. 9b) and *ii)* observed for ferrobasaltic melts in which no diffusion profiles are present (Fig. 5b), strongly suggests the influence of incomplete diffusion to the evaporating surface in increasing $^{66/64}Zn(\alpha_{vap\text{-}liq})$ during evaporation from rhyolitic and particularly arkosic melts.

5.2. Evaporation processes in natural rocks

The corollary that the rate of mass transfer of two isotopes from the evaporation surface is proportional to the ratios of the reduced masses of the evaporating species, $(\mu_{jk}/\mu_{ik})^{1/3}$, is that fractionation factors at the diffusive limit are sensitive to the mean molecular mass of the surrounding gas. In detail, isotopic fractionation is suppressed if diffusion occurs through lighter gases, and promoted for diffusion through heavier gases. Physically, this phenomenon arises because, when the difference in molar mass between two constituents is large, the collisions between the lighter molecules in a binary gas mixture govern its velocity distribution (Chapman and Cowling, 1970). This can be verified mathematically, where the reduced mass tends to that of the lighter constituent as the mass difference between the two increases, independent of their abundance ratio. In our case, as the lighter, ambient gas (k) is in excess of both evaporating species, i and j (the so-called quasi-Lorentzian condition; Mason, 1957), then, the greater the difference between m_k and $m_{i,j}$, the more the reduced masses μ_{jk} and μ_{ik} tend to a common value (m_k), and hence the closer the fractionation factor is to unity. Conversely, if $m_k >> m_{i,j}$, then the reduced mass of the mixture ik is approximated by m_i (and the mixture jk by m_j), and the fractionation factor approaches $(m_j/m_i)^{1/3}$. Figure 10 illustrates the dependence of $^{i/j}E(\alpha_{vap\text{-}liq})_{net}$ on the atmospheric molar mass (m_k) at the diffusive limit for four moderately volatile element isotope pairs.

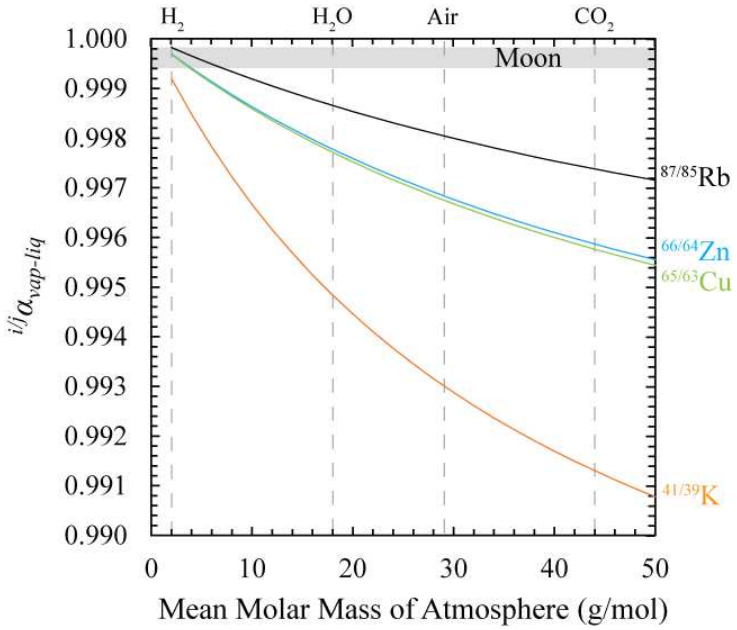

Figure 10. The modelled change of $^{i/j}E(\alpha_{vap\text{-}liq})_{net}$ at the diffusive limit for four moderately volatile element isotope pairs ($^{87/85}$Rb, black; $^{66/64}$Zn, blue; $^{65/63}$Cu, green; $^{41/39}$K, orange) evaporating as monatomic gases, as a function of the mean molar mass of the gas through which they diffuse. Common molecules or atmospheres to which these molar masses correspond are shown as dashed grey lines. The grey horizontal bar corresponds to $^{i/j}E(\alpha_{vap\text{-}liq})_{net}$ inferred for the Moon, deduced from the isotopic compositions of lunar mare basalts. In each case, the fractionation factor lies between 0.9994 and 0.9999 (see text).

5.2.1. Tektites

Samples for which the composition and total pressure of the atmosphere into which evaporation occurs is known presents the simplest scenario to understand the conditions of vaporisation in natural systems. This criterion is satisfied by tektites, glasses that formed upon melting and subsequent quenching of crustal rocks during hypervelocity impact events (Koeberl, 1986 and references therein). Because these events are recent (<35 Myr; Koeberl, 1994) up to ~790,000 years ago for Australites (Schneider et al., 1992), evaporation occurred into air with characteristics identical to those observed today.

The derivation of $^{i/j}E(\alpha_{vap\text{-}liq})_{net}$ from analyses of tektites is sensitive to the assumed composition of their source rocks. Although the Cu and Zn isotope composition of the continental crust is not expected to differ significantly from igneous rocks (at least on the scale relative to the fractionation observed in tektites), their initial concentrations may vary by more than a factor of 2 (Taylor and Kaye, 1969; Koeberl, 1986; Žák et al., 2016). Owing to the compositional similarity borne by non-volatile elements in tektites to the upper continental crust (UCC), it has been customary to use it to calculate Cu_0 and Zn_0 which yields 28 ppm and 67 ppm, respectively (Rudnick and Gao, 2003). However, source compositions among tektite groups may vary, as substantiated by the non-linear arrays in $\ln f(E)$ *vs.* $\delta^i E$ space (Moynier et al., 2009; Jiang et al., 2019), complicating the extraction of accurate $^{i/j}E(\alpha_{vap\text{-}liq})_{net}$ from these data.

Considering these uncertainties, both $^{66/64}Zn(\alpha_{vap\text{-}liq})$ and $^{65/63}Cu(\alpha_{vap\text{-}liq})$ lie in the range 0.996 to 0.999 (Moynier et al., 2009; Rodovska et al., 2017; Jiang et al., 2019), values which are broadly consistent with those predicted from our model (0.9966). The smaller fractionation of $^{66/64}Zn(\alpha_{vap\text{-}liq})$ with respect to $^{65/63}Cu(\alpha_{vap\text{-}liq})$ inferred by Moynier et al., (2010) was attributed to the slower diffusion of Zn in the tektite melt at high temperatures with respect to Cu. On the other hand, a recent measurement of and elemental profiles of Cu, Zn and K in a tektite from Hainan did not observe systematic zoning in abundance for any of the three elements. Nevertheless, the absence of zoning in the Hainan tektite (r = 0.045 m) does not necessarily exclude diffusion-limited fractionation in other tektites, as they are each

sensitive to the local formation conditions and may have also re-homogenised by convection during- or post-vaporisation. Our expression predicts no dependence of t_{evap}/t_{diff} on r for diffusion-limited conditions, meaning zoning is as likely to manifest itself in small tektites as it is in larger ones. That K isotopes do not show any measurable fractionation in tektites (Jiang et al., 2019), despite the high diffusion coefficient of K in silicate melts (Jambon, 1982) relative to Zn, instead suggests that potassium remained non-volatile; a loss of ~ 1 % of its initial budget with $^{41/39}K(\alpha_{vap\text{-}liq}) = 0.993$ would result in isotopic fractionation of + 0.07 ‰. Its lack of evaporative loss is plausibly related to its very low activity coefficient in silicate melts, ~10^{-4} (Sossi et al., 2019), and in particular those that are silica-rich (Borisov, 2009), causing a 10,000 × decrease in partial pressure relative to cases in which K behaves ideally. As such, much of the K remains in the melt, even for considerable losses of Cu and Zn.

Our experiments demonstrate that $^{66/64}Zn(\alpha_{vap\text{-}liq})$ is slightly lower (more fractionation) than $^{65/63}Cu(\alpha_{vap\text{-}liq})$ when the glass is homogeneous, opposite to that observed in tektites. This discrepancy is most readily explicable by diffusion-limited Zn isotope fractionation during evaporation due to its slower diffusion through the tektite liquid relative to Cu, as verified experimentally in Fig. 5, and modelled in section 4.1 and in Moynier et al. (2009). Indeed, core and rim analyses of a single Australite tektite (Moynier et al., 2009) show that the core is enriched in Zn (265 ppm) and light isotopes ($\delta^{66}Zn = +1.22$ ‰) relative to the rim (19 ppm and +1.83 ‰), in qualitative agreement with such a scenario. On the basis that Sn isotopes, with a similar relative mass difference, show comparable isotopic fractionation to Zn (and thus less than Cu) in the same tektites also lends support a diffusive barrier to isotope fractionation during evaporation (Creech et al., 2019).

It remains challenging to use experimental results in a uniform temperature environment to quantitatively assess isotopic fractionation in tektites. This is because, in the impact scenario that forms tektites, shocked material follows a Hugoniot before undergoing decompression that leads to fragmentation in which material intersects the liquid-vapour phase transition from the liquid side (Melosh and Vickery, 1991), meaning temperature cannot be assumed to be constant over the vaporisation timescale and steady-state conditions may have not been achieved (Humayun and Koeberl, 2004). Some authors have also appealed to a vapour-cloud produced by the impact itself in modifying the local atmospheric conditions around tektite precursors undergoing fusion and vaporisation (Rodovska et al. 2017). Further work is required to evaluate the degree and sense of internal elemental and isotope zonation within tektite glasses, together with a better estimate of their initial abundances in potential source rocks (*e.g.* Zak et al. 2016) to discriminate between the mechanisms of vaporisation during their formation.

5.2.2. The Moon

Assessment of the volatile loss that was thought to have affected the composition of the Moon following a giant impact event is subject to the opposite problem; although the fractionation factors for moderately volatile elements are well-defined, the composition of its likely atmosphere or the locus of volatile depletion are not. The separation of condensed phases from gas may have occurred during various stages of lunar formation, such as upon viscous spreading attending proto-lunar disk collapse (Canup et al. 2015), partial condensation during cooling of a synestia (Lock et al. 2018), or loss of an atmosphere in equilibrium with an early lunar magma ocean (Sossi et al. 2018; Charnoz et al. 2019). The bulk composition of the atmosphere at the vapour-liquid interface in each scenario, and the mechanisms by which volatiles are lost, are poorly constrained and are expected to have varied according to the local physico-chemical conditions. Stable isotopes may shed light on these issues, as their fractionation is sensitive to both the mode of evaporative loss and transport (*sections 4.1, 4.2*) and the thermodynamic conditions (*section 3.2*) under which volatile depletion took place.

The $^{i/j}E(\alpha_{vap\text{-}liq})_{net}$ inferred for the Moon is calculated on the basis of the elemental and isotopic compositions of lunar mare basalts, the most extensive form of magmatism exposed on the lunar surface (BVSP, 1981), which have subsequently been used to inform compositional models for the bulk Moon

(O'Neill, 1991; Taylor and Wieczorek, 2014; Ni et al., 2019). Although lunar pyroclastic glass beads have also been used for this purpose (Hauri et al., 2015; Ni et al., 2019), their utility is limited in this context because recondensation occurring during fire-fountaining has resulted in isotopic fractionation, overprinting the primary mantle signature (Moynier et al., 2006; Herzog et al., 2009). Mg Suite rocks, due to their high Mg#, pristine nature and old crystallisation ages are also useful probes of lunar interior composition (Warren, 2005; Shearer et al., 2015). Mg Suite cumulates have lower Zn contents and are more isotopically fractionated than mare basalts, with the net result being the inferred $^{66/64}Zn(\alpha_{vap\text{-}liq})$ is comparable (~0.9993) to that defined by mare basalts (0.9996) (see Day et al., 2020).

As such, the definition of a bulk lunar mantle is a conceptual construct, akin to the 'bulk silicate Earth', and should not be taken to imply that the lunar interior is homogeneous. Rather, we examine rocks of the same lithology (*i.e.*, mare basalts) for which compositional and isotopic variations are statistically similar within a given group such that they permit comparison among different elements. Then, given the isotopic and chemical similarity observed for non-volatile elements between the Earth's mantle and the lunar mantle (Warren, 2005; Zhang et al., 2012; Young et al., 2016; Sossi and Moynier, 2017; Sedaghatpour and Jacobsen, 2019), the Cu and Zn elemental and isotope compositions of the bulk silicate Earth are adopted as the compositional starting points from which lunar volatile loss is modelled. Here we investigate the $^{i/j}E(\alpha_{vap\text{-}liq})$ of four moderately volatile elements, K, Cu, Zn and Rb, for which both the isotopic and chemical composition in the lunar mantle is well constrained, as summarised in Table 4.

Table 4. A summary of the Zn, Cu, K and Rb abundances and isotopic compositions in the Earth's and Moon's mantle (based on mare basalts), and calculated vapour-Moon fractionation factors.

	Zn (ppm)	δ^{66}Zn (‰)	Cu (ppm)	δ^{65}Cu (‰)	K (ppm)	δ^{41}K (‰)	Rb (ppm)	δ^{87}Rb (‰)
Moon's mantle	2.1 ± 1	1.4 ± 0.2	11	0.68 ± 0.17	42 ± 6	-0.07 ± 0.09	0.125 ± 0.005	0.04 ± 0.09
Earth's mantle	53.5 ± 3	0.16 ± 0.06	30 ± 6	0.06 ± 0.10	260 ± 39	-0.48 ± 0.03	0.605 ± 0.060	-0.13 ± 0.06
$\ln f(E)_{Moon}$	-3.24 ± 0.39		-1.00 ± 0.22		-1.82 ± 0.28		-1.58 ± 0.13	
$\Delta^{i}E_{Moon\text{-}Earth}$	1.24 ± 0.21		0.61 ± 0.20		0.41 ± 0.09		0.17 ± 0.11	
$^{i/j}E(\alpha_{vap\text{-}Moon})$	0.9996 ± 0.0001		0.9994 ± 0.0003		0.9998 ± 0.0001		0.9999 ± 0.0001	

Palme and O'Neill (2014) – Zn, K, Rb abundances BSE; Wang and Becker (2015) – Cu abundances BSE; Taylor and Wieczorek (2014), O'Neill (1991) – Zn, K, Rb abundances Moon; Ni et al. (2019) – Zn, Cu, K abundances Moon; Paniello et al. (2012), Kato et al. (2015) – $\delta^{66}Zn_{Moon}$; Sossi et al., (2018) – $\delta^{66}Zn_{Earth}$; Herzog et al. 2009, Day et al. (2019) – $\delta^{65}Cu_{Moon}$; Liu et al. (2015) – $\delta^{65}Cu_{Earth}$; Wang and Jacobsen (2016), Tian et al. (2020) – $\delta^{41}K_{Earth,\ Moon}$; Pringle and Moynier (2017), Nie and Dauphas (2019) – $\delta^{87}Rb_{Earth,\ Moon}$.

In each case, the calculated $^{i/j}E(\alpha_{vap\text{-}liq})$ lies between 0.9994 ± 0.0002 (Cu) and 0.9999 ± 0.0001 (Rb). The diffusion-limited fractionation factor approaches these values only for an H_2-rich gas with mean molar mass ~ 2 g/mol (Fig. 10). However, such a scenario is doubtful considering that *i)* the strong temperature contrast in the proto-lunar atmosphere that would have promoted convection preventing the establishment of a diffusive gradient (Thompson and Stevenson, 1988), *ii)* a hydrogen-rich atmosphere likely never existed in the protolunar disk or early Moon due to the propensity for hydrodynamic escape to occur in its early evolution in the vicinity of the Earth's Roche Limit (Nakajima and Stevenson, 2018; Charnoz et al., 2019), *iii)* it is not clear whether the Moon's atmosphere was ever thick enough to produce total pressures that would cause evaporative loss to be diffusion-limited. Even had the Moon retained most of its hydrogen, at any reasonable oxygen fugacity in an atmosphere in equilibrium with silicate material, between the IW and FMQ buffers (Visscher and Fegley, 2013), the H_2/H_2O ratio varies between 0.5 and 0.02, respectively, such that the mean molecular mass of the gas was likely to be >10 g/mol. Figure 10 was constructed presuming that each element vaporised as a monatomic gas (*e.g.* Cu^0, Zn^0). However, in volcanic gases, Cu, Zn and the alkali metals tend to form chloride species (Symonds and Reed, 1993; Churakov et al., 2000; Renggli et al., 2017; Henley and Seward, 2018). Nevertheless, Sossi and Fegley (2018) showed that, for a steam atmosphere produced by evaporation of the bulk silicate Earth at 2000 K, $ZnCl_2$(g) and CuCl(g) form only at pressures >> 1

bar, suggesting they were unlikely to have been present in the more tenuous atmosphere of the proto-Moon at magmatic temperatures (> 1000 °C).

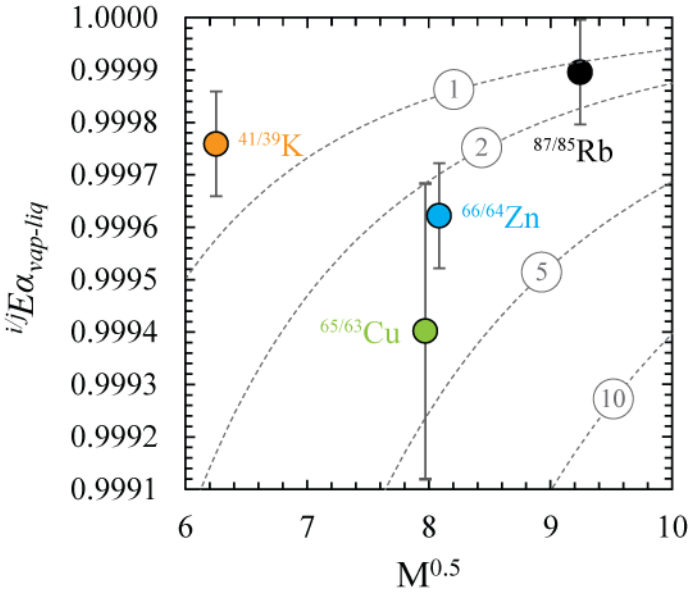

Figure 11. Best estimates for the isotopic fractionation factor of four well-defined moderately volatile elements between the Earth's mantle and the Moon's mantle against the square root of their mean molar masses. Overlain on the lunar data are grey dashed curves showing the fractionation that would arise during diffusion-limited evaporation into fictive atmospheres with different mean molar masses in g/mol (numbers in circles).

That these metals were likely present as monatomic gases suggests that, should transport phenomena have been important in causing isotopic fractionation, a correlation would be expected with molecular mass, the predominant variable controlling diffusion rates in condensed phases and gases. Figure 11 illustrates that this is not observed, strongly arguing against any kind of non-equilibrium process in setting the relative isotopic fractionations among MVEs. Fractionation factors shown in Table 3 also overlap with those calculated by *ab-initio* models, for which equilibrium values of $^{i/j}E(\alpha_{vap\text{-}liq})$ between common silicate minerals and monatomic gas range from ~ 0.9995 at 1000 K to ~ 0.9999 at 2000 K for K, Zn and Rb (Ducher et al. 2016; Li et al. 2019; Zeng et al. 2019), though the relevance of these mineral-gas fractionation factors to Moon-forming conditions remains uncertain. That equilibrium partial pressures more strongly influence lunar volatile depletion than do mass transport phenomena is also supported by the scaling of lunar element depletion factors with chemical affinity (*e.g.* O'Neill, 1991). The alkali metals evaporate according to a similar stoichiometry; where $M^{+}O_{0.5}$ (l, s) = M^{0}(g) + ¼O_2 (barring Cs, for which Cs_2O(g) is an abundant gas species; Sossi and Fegley, 2018), and are each conspicuously depleted to a similar extent in the Moon relative to Earth's mantle (a factor of 6, save for Li which is non-volatile). This commonality comes despite large differences in molar masses ($\Delta m_{\text{Rb-Na}}$ = 55.5 g/mol) that far exceed any small differences in isotopic mass ($\Delta m_{41\text{K-}39\text{K}}$ = 2 g/mol), a property that would engender elemental separation by mass transport in a gas phase (*section 4.2.*). A chemical equilibrium control on volatile element fractionation on the Moon is also supported by dynamical models of planetesimal atmospheres which suggest that equilibrium is readily attained, even at low total pressures (Young et al. 2019), and the lighter isotope compositions of Cr and Sn in the Moon (Sossi et al., 2018; Wang et al., 2019) relative to Earth's mantle, which would be violated by any mass-transport process that favours loss of the lighter isotope.

Conversely, H_2-rich gases may be instrumental in dampening isotopic fractionation in primary planetary atmospheres that evolved by accretion of nebular gas. These high-pressure, hydrogen-rich environments likely characterised accretion zones of chondrites and of the terrestrial planets < 5 Myr, the approximate timing of loss of the nebular gas to the Sun (Dauphas and Chaussidon, 2011). This phenomenon may

863 also explain why isotopic fractionation attending chondrule formation is limited in the solar nebula (*e.g.*
864 Alexander et al., 2000; Galy et al., 2000; Pringle et al., 2017), where H_2 is by far the dominant
865 constituent. Alternatively, when evaporation becomes so fast relative to the diffusion rate that t_{diff}/t_{evap}
866 tends to infinity, ${}^{i/j}\mathrm{E}(\alpha_{vap\text{-}liq})_{\mathrm{net}}$ tends to unity, which means that evaporation can occur without any
867 isotopic fractionation provided the diffusion rate in the condensed phase is very low and/or the
868 evaporation rate is very fast. These conditions may typify the evaporation of dry, siliceous silicate melts
869 or sublimation of solids in the reducing nebular gas (see also Ozawa and Nagahara, 2001). Such H-rich
870 conditions may also be expected to be present on hot, close-in exoplanets with escaping steady-state
871 atmospheres (Owen, 2019), and may serve to understand isotope ratios of volatile elements heavier than
872 hydrogen.

873

6.0. Conclusions

We establish that isotopic fractionation during evaporation of Cu and Zn from basaltic silicate melts at 1 bar, for which evaporation is not limited by diffusion in the melt, follows $^{66/64}Zn(\alpha_{vap\text{-}liq}) = 0.9959 \pm 0.0002$ and $^{65/63}Cu(\alpha_{vap\text{-}liq}) = 0.9972 \pm 0.0001$. Fractionation factors become closer to unity for lower oxygen fugacity, as the vaporisation rate increases, despite no change in vaporisation reaction stoichiometries. These experiments are zoned, and we derive diffusion rates for Cu and Zn in ferrobasalt at 1300 °C (2.61×10^{-9} m^2/s and $1.56 \pm 0.25 \times 10^{-9}$ m^2/s, respectively), that remain constant with fO_2. Thus, the ratio of the timescale of evaporation/diffusion decreases such that a heavy-isotope rich boundary layer develops at the evaporating surface of the melt at lower fO_2. This occurs because, even though the diffusion of the lighter isotope is faster than the heavier isotope by a factor $(M_j/M_i)^{\beta}$, this factor, in which $\beta \approx 0.015$, is closer to 1 than is the vapour-liquid fractionation factor at the surface. The net fractionation factor is therefore also closer to unity in cases where diffusion in the liquid is slower than evaporation, and, at the extreme, results in no isotopic fractionation for infinitesimally slow diffusion rates.

We develop a new formalism describing transport of the evaporating species in the gas phase, which dictates its ability to escape from the evaporating surface. For natural convection in the gas at 1 bar, the partial pressure of the evaporating species at the surface in a steady state is ~99% of that of its equilibrium partial pressure. Under these conditions, we show that mass loss is limited according to the diffusion rate of species i through the gas of mean molar mass k to the power of 2/3, which is itself proportional to the inverse square-root of their reduced mass, $\mu_{ik}^{-1/2}$. Isotopic fractionation between two isotopes i and j, is therefore proportional to $(\mu_{jk}/\mu_{ik})^{1/3}$. This formalism reproduces the fractionation factor of the isotopes of K, Cu and Zn in experiments of silicate melt evaporation at 1 bar in different gas mixtures to within $^{i/j}E(\alpha_{vap\text{-}liq}) \pm 0.0005$. As the fractionation factor depends on the reduced mass, it is sensitive to not only the mass of the evaporating species, but also to that of the atmosphere into which it evaporates, with heavier atmospheres promoting fractionation.

Provided that the evaporation of tektites occurs in air and at 1 bar, the isotopic fractionation recorded in Cu and Zn in these impact glasses overlaps with those predicted by our model, $^{i/(i\text{-}2)}E(\alpha_{vap\text{-}liq}) = 0.9966$. Contrastingly, the isotopic fractionation factors of semi-volatile metals for vapour loss from the Moon, as inferred from the composition of lunar mare basalts, are much closer to unity than predicted, save for if vaporisation occurred into a pure H_2 atmosphere. However, the fact that such atmospheric compositions are unlikely to have been stable on the early Moon, together with a lack of a strong mass dependence among the depletion of alkali metals or their isotopes, suggest that mass transport was not an important process in causing isotopic fractionation on the Moon.

Acknowledgements

PAS thanks the Swiss National Science Foundation Ambizione Fellowship (#180025). FM thanks the European Research Council under the H2020 scheme with the grant #637503 (PRISTINE) and the ANR through the LABEX UnivEarth. We are grateful to the Executive Editor Jeff Catalano and to Associate Editor Fang Huang for exemplary editorial handling, and to Frank Wombacher, Jian Huang and Kun Wang for their comprehensive, thorough and constructive reviews that made for a more accessible and carefully-considered article. We appreciate the assistance of Michel Fialin and Nicolas Rividi on the Microprobe, and Marcel Guillong and Pete Tollan on the Laser. We thank Mike Jollands for an introduction to finite difference modelling.

References

Ackermann R. J., Thorn R. J. and Winslow G. H. (1962) *Some fundamental aspects of vaporization*, Argonne National Laboratory, Illinois.

Alexander C. M. O., Grossman J. N., Wang J., Zanda B., Bourot-Denise M. and Hewins R. H. (2000) The lack of potassium-isotopic fractionation in Bishunpur chondrules. *Meteorit. Planet. Sci.* **35**, 859–868.

Bartlett R. W. (1967) Platinum Oxidation Kinetics with Convective Diffusion and Surface Reaction. *J. Electrochem. Soc.* **114**, 547–550.

Borisov A. A. (2009) Influence of SiO_2 and Al_2O_3 on the activity coefficients of alkalis in melts: an experimental study. *Petrology* **17**, 579.

Boss A. P. (1998) Temperatures in protoplanetary disks. *Annu. Rev. Earth Planet. Sci.* **26**, 53–80.

Boyce J. W., Kanee S. A., McCubbin F. M., Barnes J. J., Bricker H. and Treiman A. H. (2018) Early loss, fractionation, and redistribution of chlorine in the Moon as revealed by the low-Ti lunar mare basalt suite. *Earth Planet. Sci. Lett.* **500**, 205–214.

BVSP (1981) *Basaltic Volcanism Study Project*., Pergamon Press Inc., New York.

Canup R. M., Visscher C., Salmon J. and Fegley B. (2015) Lunar volatile depletion due to incomplete accretion within an impact-generated disk. *Nat. Geosci.*, **8**, 918–921.

Chapman S. and Cowling T. G. (1970) *The Mathematical Theory of Non-Uniform Gases*. 3rd ed., Cambridge University Press, Cambridge.

Charnoz S., Lee Y.-N., Sossi P. A., Allibert L., Siebert J., Hyodo R., Genda H. and Moynier F. (2019) Efficient early Moon devolatilisation just after its formation, through tidally-assisted hydrodynamic escape. In *50th Lunar and Planetary Science Conference* p. 2132.

Chilton T. H. and Colburn A. P. (1934) Mass Transfer (Absorption) Coefficients - Prediction from Data on Heat Transfer and Fluid Friction. *Ind. Eng. Chem.* **26**, 1183–1187.

Churakov S. V, Tkachenko S. I., Korzhinskii M. A., Bocharnikov R. E. and Schmulovich K. I. (2000) Evolution of composition of high temperature fumarolic gasses from Kudryavy volcano, Iturup, Kuril Islands: the thermodynamic modeling. *Geochemistry Int.* **38**, 436–451.

Craig H. (1968) Isotope separation by carrier diffusion. *Science* **159**, 93–96.

Crank J. (1975) *The mathematics of diffusion*, Clarendon Press, Oxford, UK.

Creech J. B., Moynier F. and Koeberl C. (2019) Volatile loss under a diffusion-limited regime in tektites: Evidence from tin stable isotopes. *Chem. Geol.* **528**, 119279.

Cussler E. L. (2009) *Diffusion: Mass Transfer in Fluid Systems*, Cambridge University Press, Cambridge, UK.

Dauphas N. and Chaussidon M. (2011) A Perspective from Extinct Radionuclides on a Young Stellar Object: The Sun and Its Accretion Disk. *Annu. Rev. Earth Planet. Sci.* **39**, 351–386.

Dauphas N., Janney P. E., Mendybaev R. A, Wadhwa M., Richter F. M., Davis A. M., van Zuilen M., Hines R. and Foley C. N. (2004) Chromatographic separation and multicollection-ICP-MS analysis of iron. Investigating mass-dependent and -independent isotope effects. *Anal. Chem.* **76**, 5855–63.

Davis A. M., Hashimoto A., Clayton, R. N. and Mayeda T. K. (1990) Isotope mass fractionation during evaporation of Mg_2SiO_4. *Nature* **347**, 655–658.

Day J. M. D., Kooten E. M. M. E. Van, Hofmann B. A. and Moynier F. (2020) Mare basalt meteorites

959 , magnesian-suite rocks and KREEP reveal loss of zinc during and after lunar formation. *Earth*
960 *Planet. Sci. Lett.* **531**, 115998.

961 Day J. M. D. and Moynier F. (2014) Evaporative fractionation of volatile stable isotopes and their
962 bearing on the origin of the Moon. *Philos. Trans. R. Soc. A Math. Phys. Eng. Sci.* **372**, 1–26.

963 Day J. M. D., Moynier F., Meshik A. P., Pradivtseva O. V and Petit D. R. (2017) Evaporative
964 fractionation of zinc during the first nuclear detonation. *Sci. Adv.* **3**, e1602668.

965 Day J. M. D., Sossi P. A., Shearer C. K. and Moynier F. (2019) Volatile distributions in and on the
966 Moon revealed by Cu and Fe isotopes in the " Rusty Rock " 66095. *Geochim. Cosmochim. Acta*
967 **266**, 131–143.

968 Dixon J. E., Stolper E. M. and Holloway J. R. (1995) An Experimental Study of Water and Carbon
969 Dioxide Solubilities in Mid-Ocean Ridge Basaltic Liquids. Part I: Calibrations and Solubility
970 Models. *J. Petrol.* **36**, 1607–1631.

971 Ducher M., Blanchard M. and Balan E. (2016) Equilibrium zinc isotope fractionation in Zn-bearing
972 minerals from first-principles calculations. *Chem. Geol.* **443**, 87–96.

973 Eggins S. M. and Shelley J. M. G. (2002) Compositional Heterogeneity in NIST SRM 610-617
974 Glasses. *Geostand. Geoanalytical Res.* **26**, 269–286.

975 Eucken A. (1913) Über das Wärmeleitvermögen, die spezifische Wärme und die innere Reibung der
976 Gase. *Phys. Z* **14**, 324–332.

977 Ford-Versypt A. N. and Braatz R. D. (2014) Analysis of finite difference discretization schemes for
978 diffusion in spheres with variable diffusivity. *Comput. Chem. Eng.* **71**, 241–252.

979 Frössling N. (1938) Uber die verdunstung fallernder tropfen. *Gerlands Beitr. Geophys.* **52**, 170–216.

980 Fuchs N. A. (1959) *Evaporation and droplet growth in gaseous media*, Pergamon Press, London.

981 Galy A., Young E. D., Ash R. D. and Nions R. K. O. (2000) The Formation of Chondrules at High
982 Gas Pressures in the Solar Nebula. *Science.* **290**, 1751–1754.

983 Giordano D., Russell J. K. and Dingwell D. B. (2008) Viscosity of magmatic liquids: A model. *Earth*
984 *Planet. Sci. Lett.* **271**, 123–134.

985 Guillong M., Quadt A. Von, Sakata S., Peytcheva I. and Bachmann O. (2014) LA-ICP-MS Pb – U
986 dating of young zircons from the Kos – Nisyros volcanic centre, SE Aegean arc. *J. Anal. At.*
987 *Spectrom.* **29**, 963–970.

988 Hashimoto A. (1990) Evaporation kinetics of forsterite and implications for the early solar nebula.
989 *Nature* **347**, 53–55.

990 Hauri E. H., Saal A. E., Rutherford M. J. and Van Orman J. A. (2015) Water in the moon's interior:
991 Truth and consequences. *Earth Planet. Sci. Lett.* **409**, 252–264.

992 Henley R. W. and Seward T. M. (2018) Gas–solid reactions in arc volcanoes: Ancient and modern. In
993 *Reviews in Mineralogy and Geochemistry 84* (eds. P. King, B. Fegley, and T. M. Seward).
994 Mineralogical Society of America, Geochemical Society. pp. 309–349.

995 Herzog G. F., Moynier F., Albarède F. and Berezhnoy A. A. (2009) Isotopic and elemental
996 abundances of copper and zinc in lunar samples, Zagami, Pele's hairs, and a terrestrial basalt.
997 *Geochim. Cosmochim. Acta* **73**, 5884–5904.

998 Hoenig C. L. and Searcy A. W. (1966) Knudsen and Langmuir Evaporation Studies of Stannic Oxide.
999 *J. Amer. Ceram. Soc.* **49**, 128–134.

1000 Holzheid A. and Lodders K. (2001) Solubility of copper in silicate melts as function of oxygen and
1001 sulfur fugacities, temperature, and silicate composition. *Geochim. Cosmochim. Acta* **65**, 1933–

1951.

Humayun M. and Cassen P. (2000) Processes Determining the Volatile Abundances of the Meteorites and Terrestrial Planets. In *The Origin of the Earth and Moon* (eds. R. M. Canup and K. Righter). University of Arizona Press, Tucson. pp. 3–23.

Humayun M. and Clayton R. N. (1995) Potassium isotope cosmochemistry: Genetic implications of volatile element depletion. *Geochim. Cosmochim. Acta* **59**, 2131–2148.

Humayun M. and Koeberl C. (2004) Potassium isotopic composition of Australasian tektites. *Meteorit. Planet. Sci.* **39**, 1509–1516.

Janney P. E., Mendybaev R. A., Dauphas N., Davis A. M., Richter F. M. and Wadhwa M. (2004) "Nonideal" isotopic fractionation behaviour of magnesium in evaporation residues. In *Lunar and Planetary Science Conference XXXV* p. 2092.

Jiang Y., Chen H., Fegley B., Lodders K., Hsu W., Jacobsen S. B. and Wang K. (2019) Implications of K , Cu and Zn isotopes for the formation of tektites. *Geochim. Cosmochim. Acta* **259**, 170–187.

Kamber B.S. & Schoenberg R. (2020) Evaporative loss of moderately volatile metals from the superheated 1849 Ma Sudbury impact melt sheet inferred from stable Zn isotopes. *Earth Planet. Sci. Lett.* **544**, 116356.

Kato C., Moynier F., Valdes M. C., Dhaliwal J. K. and Day J. M. D. (2015) Extensive volatile loss during formation and differentiation of the Moon. *Nat. Commun.* **6**, 7617.

Knacke O. and Stranski I. N. (1952) The mechanism of evaporation. *Prog. Met. Phys.*, 181–235.

Knight K. B., Kita N. T., Mendybaev R. A., Richter F. M., Davis A. M. and Valley J. W. (2009) Silicon isotopic fractionation of CAI-like vacuum evaporation residues. *Geochim. Cosmochim. Acta* **73**, 6390–6401.

Knudsen M. (1909) Die Gesetze der Molekularströmung und der inneren Reibungsströmung der Gase durch Röhren. *Ann. Phys.* **333**, 75–130.

Koeberl C. (1986) Geochemistry of tektites and impact glasses. *Annu. Rev. Earth Planet. Sci.* **14**, 323–350.

Koeberl C. (1994) Tektite origin by hypervelocity asteroidal or cometary impact. *Large Meteor. Impacts Planet. Evol.* **293**, 133.

Lamoreaux R. H., Hildenbrand D. L. and Brewer L. (1987) High-Temperature Vaporization Behavior of Oxides II. Oxides of Be, Mg, Ca, Sr, Ba, B, Al, Ga, In, Tl, Si, Ge, Sn, Pb, Zn, Cd, and Hg. *J. Phys. Chem. Ref. Data* **16**, 419.

Langmuir I. (1916) The evaporation, condensation and reflection of molecules and the mechanism of adsorption. *Phys. Rev.* **8**, 149–176.

Li Y., Wang W., Wu Z., and Huang S. (2019) First-principles investigation of equilibrium K isotope fractionation among K-bearing minerals. *Geochim. Cosmochim. Acta*, **264**, 30–42.

Liu S. A., Huang J., Liu J., Wörner G., Yang W., Tang Y. J., Chen Y., Tang L., Zheng J. and Li S. (2015) Copper isotopic composition of the silicate Earth. *Earth Planet. Sci. Lett.* **427**, 95–103.

Liu T. and Bautista R. G. (1981) Prediction of the Global Volatilization Rate of Gas-Metal-Alloy Reaction Systems-Method of Calculation. *Oxid. Met.* **16**, 243–252.

Lock S. J., Stewart S. T., Petaev M. I., Leinhardt Z., Mace M. T., Jacobsen S. B., and Cuk M. (2018) The origin of the Moon within a terrestrial synestia. *J. Geophys. Res.: Planets* **123**, 910–951

Lowry R. K., Henderson P. and Nolan J. (1982) Tracer diffusion of some alkali, alkaline-earth and

transition element ions in a basaltic and an andesitic melt, and the implications concerning melt structure. *Contrib. to Mineral. Petrol.* **80**, 254–261.

Luck J.-M., Othman D. Ben and Albarède F. (2005) Zn and Cu isotopic variations in chondrites and iron meteorites: Early solar nebula reservoirs and parent-body processes. *Geochim. Cosmochim. Acta* **69**, 5351–5363.

Mason E. A. (1957) Higher Approximations for the Transport Properties of Binary Gas Mixtures. II. Applications. *J. Chem. Phys.* **27**, 782–790.

Melosh H. J. and Vickery A. M. (1991) Melt droplet formation in energetic impact events. *Nature* **350**, 494 – 497.

Mendybaev R. A., Williams C. D., Spicuzza M. J., Richter F. M., Valley J. W., Fedkin A. V and Wadhwa M. (2017) Thermal and chemical evolution in the early Solar System as recorded by FUN CAIs : Part II – Laboratory evaporation of potential CMS-1 precursor material. *Geochim. Cosmochim. Acta* **201**, 49–64.

Moynier F., Albarède F. and Herzog G. F. (2006) Isotopic composition of zinc, copper, and iron in lunar samples. *Geochim. Cosmochim. Acta* **70**, 6103–6117.

Moynier F., Beck P., Jourdan F., Yin Q. Z., Reimold U. and Koeberl C. (2009) Isotopic fractionation of zinc in tektites. *Earth Planet. Sci. Lett.* **277**, 482–489.

Moynier F., Koeberl C., Beck P., Jourdan F. and Telouk P. (2010) Isotopic fractionation of Cu in tektites. *Geochim. Cosmochim. Acta* **74**, 799–807.

Mungall J. E. (2002) Empirical models relating viscosity and tracer diffusion in magmatic silicate melts. *Geochim. Cosmochim. Acta* **66**, 125–143.

Nakajima M. and Stevenson D. J. (2018) Inefficient volatile loss from the Moon-forming disk: Reconciling the giant impact hypothesis and a wet Moon. *Earth Planet. Sci. Lett.* **487**, 117–126.

Ni P. and Zhang Y. (2016) Cu diffusion in a basaltic melt. *Am. Mineral.* **101**, 1474–1482.

Ni P., Zhang Y., Chen S. and Gagnon J. (2019) A melt inclusion study on volatile abundances in the lunar mantle. *Geochim. Cosmochim. Acta* **249**, 17–41.

Nie N. X. and Dauphas N. (2019) Vapor Drainage in the Protolunar Disk as the Cause for the Depletion in Volatile Elements of the Moon. *Astrophys. J. Lett.* **884**, L48.

O'Neill H. S. C. (1991) The origin of the moon and the early history of the earth—A chemical model. Part 2: The earth. *Geochim. Cosmochim. Acta* **55**, 1159–1172.

O'Neill H. S. C. and Eggins S. M. (2002) The effect of melt composition on trace element partitioning: an experimental investigation of the activity coefficients of FeO, NiO, CoO, MoO_2 and MoO_3 in silicate melts. *Chem. Geol.* **186**, 151–181.

Owen J. E. (2019) Atmospheric Escape and the Evolution of Close-in Exoplanets. *Annu. Rev. Earth Planet. Sci.* **47**, 67–90.

Ozawa K. and Nagahara H. (2001) Chemical and isotopic fractionations by evaporation and their cosmochemical implications. *Geochim. Cosmochim. Acta* **65**, 2171–2199.

Palme H., Larimer J. W. and Lipschutz M. E. (1988) Moderately Volatile Elements. In *Meteorites and the Early Solar System* (eds. J. F. Kerridge and M. S. Matthews). University of Arizona Press, Tucson. pp. 436–461.

Palme H. and O'Neill H. S. C. (2014) Cosmochemical Estimates of Mantle Composition. In *Treatise on Geochemistry, Vol. 3: The Mantle and Core* (ed. R. W. Carlson). Elsevier B.V., Amsterdam. pp. 1–39.

Paniello R. C., Day J. M. D. and Moynier F. (2012) Zinc isotopic evidence for the origin of the Moon. *Nature* **490**, 376–9.

Penner S. S. (1952) On the Kinetics of Evaporation. *J. Phys. Chem.* **56**, 475–479.

Poitrasson F., Halliday A. N., Lee D.-C., Levasseur S. and Teutsch N. (2004) Iron isotope differences between Earth, Moon, Mars and Vesta as possible records of contrasted accretion mechanisms. *Earth Planet. Sci. Lett.* **223**, 253–266.

Pringle E. A. and Moynier F. (2017) Rubidium isotopic composition of the Earth, meteorites, and the Moon: Evidence for the origin of volatile loss during planetary accretion. *Earth Planet. Sci. Lett.* **473**, 62–70.

Pringle E. A., Moynier F., Beck P., Paniello R. and Hezel D. C. (2017) The origin of volatile element depletion in early solar system material: Clues from Zn isotopes in chondrules. *Earth Planet. Sci. Lett.* **468**, 62–71.

Ranz W. E. and Marshall, W. R. (1952) Evaporation from Drops. Part I. *Chem. Eng. Prog.* 48, 141–146.

Rappé A. K., Casewit C. J., Colwell K. S., Goddard W. A. and Skiff W. M. (1992) UFF, a full periodic table force field for molecular mechanics and molecular dynamics simulations. *J. Am. Chem. Soc.* **114**, 10024–10035.

Renggli C. J., King P. L., Henley R. W. and Norman M. D. (2017) Volcanic gas composition, metal dispersion and deposition during explosive volcanic eruptions on the Moon. *Geochim. Cosmochim. Acta* **206**, 296–311.

Richter F. M. (2004) Timescales determining the degree of kinetic isotope fractionation by evaporation and condensation. *Geochim. Cosmochim. Acta* **68**, 4971–4992.

Richter F. M., Dauphas N. and Teng F.-Z. (2009) Non-traditional fractionation of non-traditional isotopes: Evaporation, chemical diffusion and Soret diffusion. *Chem. Geol.* **258**, 92–103.

Richter F. M., Davis A. M., Ebel D. S. and Hashimoto A. (2002) Elemental and isotopic fractionation of type B calcium-, aluminum-rich inclusions: Experiments, theoretical considerations, and constraints on their thermal evolution. *Geochim. Cosmochim. Acta* **66**, 521–540.

Richter F. M., Janney P. E., Mendybaev R. A., Davis A. M. and Wadhwa M. (2007) Elemental and isotopic fractionation of Type B CAI-like liquids by evaporation. *Geochim. Cosmochim. Acta* **71**, 5544–5564.

Richter F. M., Mendybaev R. A., Christensen J. N., Ebel D. and Gaffney A. (2011) Laboratory experiments bearing on the origin and evolution of olivine-rich chondrules. *Meteorit. Planet. Sci.* **46**, 1152–1178.

Rodovská Z., Magna T., Žák K., Kato C., Savage P. S., Moynier F., Skála R. and Jezek J. (2017) Implications for behavior of volatile elements during impacts — Zinc and copper systematics in sediments from the Ries impact structure and central European tektites. *Meteorit. Planet. Sci.* **52**, 2178–2192.

Rudnick R. L. and Gao S. (2003) Composition of the Continental Crust. In *Treatise on Geochemistry Vol. 3* (ed. R. L. Rudnick). Elsevier, Amsterdam. pp. 1–64.

Schneider D. A., Kent D. V and Mello G. A. (1992) A detailed chronology of the Australasian impact event, the Brunhes-Matuyama geomagnetic polarity reversal, and global climate change. *Earth Planet. Sci. Lett.* **111**, 395–405.

Sedaghatpour F. and Jacobsen S. B. (2019) Magnesium stable isotopes support the lunar magma ocean cumulate remelting model for mare basalts. *Proc. Natl. Acad. Sci.* **116**, 73–78.

Sharp Z. D., Shearer C. K., McKeegan K. D., Barnes J. D. and Wang Y. Q. (2010) The chlorine isotope composition of the moon and implications for an anhydrous mantle. *Science.* **329**, 1050–1053.

Shearer C. K., Elardo S. M., Petro N. E., Borg L. E. and McCubin F. M. (2015) Origin of the lunar highlands Mg-suite: An integrated petrology, geochemistry, chronology, and remote sensing perspective. *Am. Mineral.* **100**, 294–325.

Shornikov S. I. (2015) Vaporization coefficients of oxides contained in the melts of Ca-Al-inclusions in chondrites. *Geochemistry Int.* **53**, 1080–1089.

Sossi P. A. and Fegley B. (2018) Thermodynamics of Element Volatility and its Application to Planetary Processes. In *Reviews in Mineralogy and Geochemistry 84: High temperature gas-solid reactions in Earth and planetary processes* (eds. P. L. King, T. M. Seward, and B. Fegley). Mineralogical Society of America, Chantilly. pp. 393–459.

Sossi P. A., Halverson G. P., Nebel O. and Eggins S. M. (2015) Combined Separation of Cu, Fe and Zn from Rock Matrices and Improved Analytical Protocols for Stable Isotope Determination. *Geostand. Geoanalytical Res.* **39**, 129–149.

Sossi P. A., Klemme S., O'Neill H. S. C., Berndt J. and Moynier F. (2019) Evaporation of moderately volatile elements from silicate melts: experiments and theory. *Geochim. Cosmochim. Acta* **260**, 204–231.

Sossi P. A. and Moynier F. (2017) Chemical and isotopic kinship of iron in the Earth and Moon deduced from the lunar Mg-Suite. *Earth Planet. Sci. Lett.* **471**, 125–135.

Sossi P. A., Moynier F. and van Zuilen K. (2018) Volatile loss following cooling and accretion of the Moon revealed by chromium isotopes. *Proc. Natl. Acad. Sci.* **115**, 10920–10925.

Sossi P. A., Nebel O., O'Neill H. S. C. and Moynier F. (2018) Zinc isotope composition of the Earth and its behaviour during planetary accretion. *Chem. Geol.* **477**, 73–84.

Stevenson R. J., Bagdassarov N. S., Dingwell D. B. and Romano C. (1998) The influence of trace amounts of water on the viscosity of rhyolites. *Bull. Volcanol.* **60**, 89–97.

Symonds R. B. and Reed M. H. (1993) Calculation of Multicomponent chemical equilibria in gas-solid-liquid systems: Calculation methods, thermochemical data, and applications to studies of high-temperature volcanic gases with examples from Mount St. Helens. *Am. J. Sci.* **293**, 758–864.

Taylor G. J. and Wieczorek M. A. (2014) Lunar bulk chemical composition: a post-Gravity Recovery and Interior Laboratory reassessment. *Philos. Trans. R. Soc. A Math. Phys. Eng. Sci.* **372**, 20130242.

Taylor S. R. and Kaye M. (1969) Genetic significance of the chemical composition of tektites : A review. *Geochim. Cosmochim. Actamica Acta* **33**, 1083–1100.

Thompson C. and Stevenson D. J. (1988) Gravitational Instability in Two-Phase Disks and the Origin of the Moon. *Astrophys. J.* **333**, 452–481.

Tian Z., Jolliff B. L., Korotev R. L., Fegley B., Lodders K., Day J. M., Chen H., and Wang K. (2020). Potassium isotopic composition of the Moon. *Geochim. Cosmochim. Acta* **280**, 263–280.

Visscher C. and Fegley B. (2013) Chemistry of impact-generated silicate melt-vapor debris disks. *ApJ Lett.* **767**, L12.

Wang J., Davis A. M., Clayton R. N., Mayeda T. K. and Hashimoto A. (2001) Chemical and isotopic fractionation during the evaporation of the FeO-MgO-SiO_2-CaO-Al_2O_3-TiO_2 rare earth element melt system. *Geochim. Cosmochim. Acta* **65**, 479–494.

Wang K. and Jacobsen S. B. (2016) Potassium Isotopic Evidence for the Origin of the Moon. *Nature* **538**, 487–490.

Wang X., Fitoussi C., Bourdon B., Fegley B. and Charnoz S. (2019) Tin isotopes indicative of liquid-vapour equilibration and separation in the Moon-forming disk. *Nat. Geosci.* **12**, 707–712.

Wang Z. and Becker H. (2015) Abundances of Ag and Cu in mantle peridotites and the implications for the behavior of chalcophile elements in the mantle. *Geochim. Cosmochim. Acta* **160**, 209–226.

Warren P. H. (2005) "New" lunar meteorites- Implications for composition of the global lunar surface, lunar crust and the bulk Moon. *Meteorit. Planet. Sci.* **40**, 477–506.

Wimber R. T., Hills S. W., Wahl N. K. and Tempero C. R. (1977) Kinetics of Evaporation / Oxidation of Iridium. *Metall. Trans. A* **8A**, 193 – 199.

Wimpenny J., Marks N., Knight K., Rolison J. M., Borg L., Eppich G., Badro J., Ryerson F. J., Sanborn M., Huyskens M. H. and Yin Q. (2019) Experimental determination of Zn isotope fractionation during evaporative loss at extreme temperatures. *Geochim. Cosmochim. Acta* **259**, 391–411.

Wombacher F., Rehkämper M. and Mezger K. (2004) Determination of the mass-dependence of cadmium isotope fractionation during evaporation. *Geochim. Cosmochim. Acta* **68**, 2349–2357.

Wombacher F., Rehkämper M., Mezger K., Bischoff A. and Münker C. (2008) Cadmium stable isotope cosmochemistry. *Geochim. Cosmochim. Acta* **72**, 646–667.

Wombacher F., Eisenhauer A., Böhm F., Gussone N., Regenberg M., Dullo W. C. and Rüggeberg A. (2011) Magnesium stable isotope fractionation in marine biogenic calcite and aragonite. *Geochim. Cosmochim. Acta* **75**, 5797–5818.

Young E. D. (2000) Assessing the implications of K isotope cosmochemistry for evaporation in the preplanetary solar nebula. *Earth Planet. Sci. Lett.* **183**, 321–333.

Young E. D. and Galy A. (2004) The isotope geochemistry and cosmochemistry of magnesium. *Rev. Mineral. Geochem.* **55**, 197–230.

Young E. D., Kohl I. E., Warren P. H., Rubie D. C., Jacobson S. A. and Morbidelli A. (2016) Oxygen isotopic evidence for vigorous mixing during the Moon-forming giant impact. *Science* **351**, 493–496.

Young E. D., Shahar A., Nimmo F., Schlichting H. E., Schauble E. A., Tang H. and Labidi J. (2019) Near-equilibrium isotope fractionation during planetesimal evaporation. *Icarus* **323**, 1–15.

Yu Y., Hewins R. H., Alexander C. M. O. D. and Wang J. (2003) Experimental study of evaporation and isotopic mass fractionation of potassium in silicate melts. *Geochim. Cosmochim. Acta* **67**, 773–786.

Žák K., Skála R., Řanda Z., Mizera J., Heissig K., Ackerman L., Ďurišová J., Jonášová Š., Kameník J. and Magna T. (2016) Chemistry of tertiary sediments in the surroundings of the ries impact structure and moldavite formation revisited. *Geochim. Cosmochim. Acta* **179**, 287–311.

Zeng H., Rozsa V. F., Nie N. X., Zhang Z., Pham T. A., Galli G. and Dauphas N. (2019). *Ab Initio* calculation of equilibrium isotopic fractionations of potassium and rubidium in minerals and water. *ACS Earth Space Chem.* **3**, 2601–2612.

Zhang J., Dauphas N., Davis A. M., Leya I. and Fedkin A. (2012) The proto-Earth as a significant source of lunar material. *Nat. Geosci.* **5**, 251–255.